Discovery of Dynamical Heterogeneity
in a Supercooled Magnetic Monopole Fluid

Jahnatta Dasini[†1], Chaia Carroll[†1], Chun-Chih Hsu[2], Hiroto Takahashi[2],
Jack Murphy[1], Sudarshan Sharma[4], Catherine Dawson[1], Fabian Jerzembeck[2,3],
Stephen J. Blundell[2], Graeme Luke[4], J.C. Séamus Davis[1,2,3,5] and Jonathan Ward[1]

1. *Department of Physics, University College Cork, Cork T12 R5C, Ireland*
2. *Clarendon Laboratory, Oxford University, Parks Road, Oxford, OX1 3PU, UK*
3. *Max-Planck Institute for Chemical Physics of Solids, D-01187 Dresden, Germany*
4. *McMaster University, Hamilton Ontario, Canada*
5. *LASSP, Department of Physics, Cornell University, Ithaca, NY 14853, USA*
† *Contributed equally to this project*

ABSTRACT Dynamical heterogeneity[1,2,3], in which transitory local fluctuations occur in the conformation and dynamics of constituent particles, is essential for evolution of supercooled liquids[4,5,6] into the glass state[12]. Yet its microscopic spatiotemporal phenomenology has remained unobservable in virtually all supercooled glass forming liquids. Recent theoretical advances predict that corresponding dynamical heterogeneity[7-11] could also occur in supercooled[12] magnetic monopole fluids[13,14,15]. Motivated thus, we searched for dynamical heterogeneity when entering the supercooled monopole fluid of $Dy_2Ti_2O_7$. By measuring microsecond-resolved spontaneous magnetization noise $M(t,T)$ at temperatures between $15\,\text{mK} < T < 2500\,\text{mK}$ we discover a sharp bifurcation in monopole noise[16,17] characteristics beginning below $T \approx 1500$ mK, with the appearance of powerful monopole current bursts. This unique new form of dynamical heterogeneity first emerges upon entering the supercooled monopole fluid regime, reaches maximum intensity near $T \approx 500\,\text{mK}$ and then terminates along with coincident loss of ergodicity near $T \lesssim 250$ mK. Surprisingly, however, low intensity monopole noise representing activity at approximately 2% of the Dy sites persists below $T \lesssim 250$ mK, implying a population of dynamical monopoles trapped within the spin-ice ground state as $T \rightarrow 0$. This overall phenomenology significantly expands our knowledge of both supercooled monopole fluids[7-12] and of the ground state of spin-ice[7-11,13-15]. More generally, we demonstrate how comprehensive direct detection of the time sequence, magnitude and statistics of dynamical heterogeneity can greatly accelerate fundamental vitrification studies[1-6].

"The deepest and most interesting unsolved problem in solid state theory is probably the theory of the nature of glass and the glass transition" P. W. Anderson[18]. Although most pure liquids crystallize at their melting temperature, glass-forming liquids instead first enter the supercooled state[1,2,3] and eventually transition into a glass state. During this evolution it is widely hypothesized that the dynamics of constituent particles slow down radically and in an increasingly heterogeneous fashion[1,2,4,5,6], so that local regions relax on different trajectories at different rates in a continuously evolving fashion. Such dynamically heterogeneous transients are continuously occurring thermally activated[19-24] events about an unchanging thermodynamic equilibrium[1,2,6]. How their atomic-scale phenomenology controls the vitrification process remains an intense focus of research[1-6]. Current theoretical progress includes predictions of frequency-resolved loss of ergodicity[25]; of trapped nanoscale droplets with internal fluidic particle dynamics[26]; and of evolution from supercooled dynamical heterogeneity through the glass transition[27]. Only recently, however, have such phenomena been hypothesized to occur[7-11] upon cooling the magnetic monopole fluids of spin-ice.

The most pertinent material is $Dy_2Ti_2O_7$ which contains a sub-lattice of corner-sharing tetrahedra, each having a magnetic Dy^{3+} ion at its four vertices. The Dy magnetic moments ($\mu \approx 10\,\mu_B$) are Ising-like, being constrained to point along their local [111] directions towards or away from the tetrahedron center. The consequent dipolar spin-ice Hamiltonian is[28]

$$H = -J \sum_{<ij>} \boldsymbol{S}_i \cdot \boldsymbol{S}_j + Da^3 \sum_{i<j} \left(\frac{\boldsymbol{S}_i \cdot \boldsymbol{S}_j}{|\boldsymbol{r}_{ij}|^3} - \frac{3(\boldsymbol{S}_i \cdot \boldsymbol{r}_{ij})(\boldsymbol{S}_j \cdot \boldsymbol{r}_{ij})}{|\boldsymbol{r}_{ij}|^5} \right) \tag{1}$$

Here $\boldsymbol{S}_i$ represent the Ising spin at each Dy site, $\boldsymbol{r}_{ij}$ are the inter-site distances, $J \approx 1.1$ K is the exchange energy, $D = \mu_0\mu^2/(4\pi a^3)$ the nearest-neighbor dipole interaction energy, and *a* is the nearest-neighbor distance between moments. From Eqn. 1, only six possible ground-state spin configurations exist on each tetrahedron, all being 2-in:2-out spin arrangements[29]. Although the dipole interactions in Eqn. 1 should stabilize long-range magnetic order[30] near $T \approx 200$ mK, no such state is observed to below $T \approx 50$ mK[31]. Hence, the actual $T \to 0$ state of pyrochlore spin-ice, and the monopole kinetics generating it, remain a focus of intense research[7-15].

By contrast, the excited states governed by Eqn. 1 at higher temperatures are well understood[13,14,15] to be mobile magnetic charges (monopoles) of both signs: $+m$ for 1-in:3-out and $-m$ for 3-in:1-out. They exist in a magnetic-charge neutral fluid in which equal numbers of $+m$ and $-m$ are thermally excited across the Dy spin-flip energy barrier $\Delta \approx 4$ K. However, below $T \approx 1.5$ K this monopole fluid enters a supercooled state[12]. Here, the

magnetic susceptibility exhibits a Havriliak-Negami (HN) form[12] characteristic of supercooled glass forming liquids[6]. Further, the relaxation time $\tau(T) = A\exp(DT_0/(T - T_0))$ where D is the 'fragility' index, diverges at $T_0 \approx 240$ mK $\pm$ 30 mK on a Vogel–Tammann–Fulcher (VTF) trajectory[12] characteristic of supercooling[4,5,6]. Additionally, Monte Carlo simulations[32] predicting magnetization noise with spectral density $S_M(\omega,T) \propto \tau(T)/(1 + (\omega\tau(T)^b)$ led to the discovery[16] of magnetic monopole noise exhibiting $b(T) \approx 1.5$[16,17]. Because this is consistent with advanced monopole transport theories based on fractal percolative clusters[9] (FPC) of monopole trajectories, heterogeneous monopole transport dynamics is construed. The broad distribution of $\chi(\omega,T)$ relaxation times, the VTF form measured for $\tau(T)$, and the monopole noise power-law, all imply by analogy with general supercooled glass-forming liquids[1-6] that monopole dynamical heterogeneity should exist in Dy$_2$Ti$_2$O$_7$.

An array of theories[7-11] have focused on monopole kinetics approaching the $T \rightarrow 0$ state of spin-ice. For all the high-temperature state is a thermally activated plasma of quasi-free monopoles[13,14,15] (state I). Refrigeration from state I is anticipated[7,9,10,11] to yield a supercooled monopole fluid (state II) sustaining some form of dynamical heterogeneity. Extended spin-ice models predict growing dynamical heterogeneity resulting in loss of ergodicity near $T/J \approx 0.1$ when spin-spin correlation time diverges[7]; similarly, dumbbell spin-ice models predict that enhancing dynamical heterogeneity near $T \approx 400$ mK in Dy$_2$Ti$_2$O$_7$, should cause the ratio $\omega S(\omega,T)/T \chi''(\omega,T)$ to diverge from its ergodic high-temperature limit[10]. Finally, analysis of $T \rightarrow 0$ state III using extended spin-ice models, yields predictions of quantum dynamical monopoles persisting as $T \rightarrow 0$ at approximately 2% of Dy sites[7]. However, the empirical phenomenology of monopole dynamics in states II and III are virtually unknown.

Recent theoretic advances predict a specific new form of heterogeneous monopole dynamics based on the existence of two spin-dynamical time-scales[9]. This constrains the trajectories of each monopole to a nanoscale FPC, a concept now well supported by experiment[9,16,17]. However, in the supercooled state II where monopole density is low, as each monopole traverses a unique FPC its interactions with the local spin environment are predicted to 'unblock'[9] the motion of other monopoles in adjacent FPCs. As the time periods for which FPCs remain blocked diverge[9] towards T$_0$, a single sudden FPC unblocking may trigger sequential cascades of FPC releases of different sizes, resulting in a wide range of monopole current bursts. This unique new form of atomic-scale dynamical heterogeneity is specific to supercooled monopole fluids[9].

To search for such phenomena in Dy$_2$Ti$_2$O$_7$, we use SQUID-based flux-noise spectrometry with magnetic field sensitivity $\delta B = \mu_0 \delta M \leq 10^{-14}$ T/$\sqrt{\text{Hz}}$ using the

apparatus shown schematically in Fig. 1a (Methods section 2). Here L_p is the inductance of both the sample pickup coil and of a counter wound compensation coil, L_i is a SQUID-input coil inductance, and $\mathcal{M}_i$ is a mutual inductance to SQUID. Our spectrometer is operated on a cryogen-free dilution refrigerator in the range $15\text{ mK} \lesssim T \lesssim 2500\text{ mK}$. The time-sequence of the magnetic flux generated by the sample, $\Phi_p(t)$, is measured with microsecond precision using a persistent superconducting circuit that transforms it into the flux $\Phi(t)$ at the SQUID input coil

$$\Phi(t) = (\mathcal{M}_i/(2L_p + L_i))\Phi_p(t) \qquad (2)$$

The SQUID output voltage $V(t) = G\Phi(t)$ where G is total gain of the electronics, is then related to magnetization as $V(t) \equiv M(t)/C_0$ where the value of C_0 can be calibrated accurately for a given experimental geometry (Methods section 2). The time-sequences of magnetization fluctuations $M(t, T) \equiv C_0 V(t)$ are recorded from whence the power spectral density of magnetization noise is $S_M(\omega, T) \equiv C_0{}^2 S_V(\omega, T)$. The separately measured noise contribution of the superconductive circuitry and SQUID are always first subtracted. The magnetic susceptibility $\chi(\omega, T)$ is measured simultaneously with $S_M(\omega, T)$ using a single spectrometer over the temperature range $15\text{ mK} < T < 2500\text{ mK}$ (Methods section 2).

For an ergodic monopole fluid, the fluctuation-dissipation theorem (FDT) linking $S_M(\omega, T)$ to the imaginary magnetic susceptibility $\chi''(\omega, T)$ would predict[10]

$$S_M(\omega, T) = 2k_\mathrm{B}T\,\chi''(\omega, T)/\omega\pi v\mu_0 \qquad (3)$$

where v is the sample volume, k_B is Boltzmann's constant, μ_0 the permeability of vacuum and we use SI units throughout. For our $Dy_2Ti_2O_7$ samples, a typical simultaneously measured $\chi'(\omega, T)$, $\chi''(\omega, T)$ and $S_M(\omega, T)$ are plotted in Fig. 1b (Methods section 3). Here, because of the wide distribution of microscopic relaxation times[12] (Methods section 1), even when $\tau(T)$ diverges, high frequency monopole dynamics must still be present at a subset of sites. Hence, to explore the evolution of Eqn. 3 to lowest temperatures, we plot in Fig. 1c the measured $S_M(\omega, T)$ versus independently measured $2k_\mathrm{B}T\,\chi''(\omega, T)/\omega\pi v\mu_0$ at frequencies where dynamics is manifestly occurring in the monopole noise. Evidently, the fluctuation-dissipation theorem holds for $T \gtrsim 500$ mK. However, because of the departure of $X(\omega, T) \equiv S_M(\omega, T)\omega\pi v\mu_0 / 2k_\mathrm{B}T\,\chi''(\omega, T)$ from 1 starting near $T \lesssim 500$ mK, the monopole fluid here slowly exits the ergodic regime. Eventually FDT is strongly violated with complete loss of monopole ergodicity $T \lesssim 250$ mK (Fig. 1c , Methods section 4).

A key signature of monopole dynamical heterogeneity would be random and intense monopole current bursts[9,11]. Hence, we next measure the time-sequences of flux threading the sample at its pickup coil, $\Phi_p(t, T)$. These are recorded from $V(t, T)$ in the form $\Phi_p(t, T) = V(t, T)/G(\mathcal{M}_i/(2L_p + L_i))$ from Eqn. 2. If each monopole exhibits a magnetic-charge m and total magnetic flux $\Phi_m = m\mu_o$[14], and because the magnetic flux through any superconductive closed-loop circuit is quantized, when a magnetic monopole passes through such a loop it

generates a supercurrent exactly counterbalancing Φ_m. This is detectable by a SQUID as a flux generated elsewhere in the circuit. Under these circumstances, the net monopole current (Methods section 5) through the pickup coil is[33]

$$J(t,T) \equiv \dot{\Phi}_p(t,T)/\mu_0 \qquad (4)$$

For measurements of $J(t)$ from $\dot{\Phi}_p(t)$ we use an 80 μs box-car average, with typical measured time sequences of $|J(t)|$ shown in Fig. 2a. The probability distribution of $|J(t)|$ is shown in Fig. 2b, wherein monopole currents range in intensity over almost five orders of magnitude with maximum intensity occurring near $T = 900$ mK. The temperature dependence of the rate of occurrence $r_{|J|}$ of monopole currents with magnitude $|J|$ is presented in Fig. 2c, while the average intensity of monopole current $\overline{|J|}(T)$ is shown in Fig. 2d. Although not manifest here, there are two populations of monopole currents, those related to conventional monopole noise and intense current bursts existing over extended time periods producing large excursions in $\Phi_p(t)$ (Methods section 5). A strong maximum in monopole current burst intensity occurs entering the supercooled regime, followed by a rapid fall and disappearance below $T \lesssim 250$ mK. Intense current bursts always involve the simultaneous motion of large numbers of monopoles in the same direction followed by a coordinated reverse monopole current a fraction of a second later (Fig. 2a). The simplest and most logical explanation is that such rapid intense cooperative dynamics of multiple monopoles occurs locally in space, where their mutual proximity allows their coordination in time.

As to the energetics of this dynamic heterogeneity, Fig. 3a provides a typical example of magnetization fluctuations in terms of $\Phi_p(t)$, with the typical background $\Phi_p(t)$ absent of any sample shown in black. The energy ε associated with each monopole configuration can be determined accurately since

$$\varepsilon(t) \equiv \Phi_p^2(t,T)/2L_p \qquad (5)$$

(Methods section 5). Typical examples of measured $\Phi_p^2(t,T)$ are shown in Fig. 3b over a representative set of temperatures. Typical histograms of the rate of occurrence $r(\varepsilon)$ of states with energy ε are presented in Fig. 3c, where each $r(\varepsilon, T)$ is acquired in a continuous 1000 second time interval at fixed T (see Supplementary Video 1). Strikingly, while the energetics $\varepsilon(t)$ are gaussian and narrow in distribution for $T \gtrsim 1500$ mK, at lower temperatures a sharp bifurcation occurs into a bi-modal distribution containing less frequent highly energetic events, each exemplifying a monopole-current burst. Eventually below $T \lesssim 250$ mK these phenomena disappear, and a low energy gaussian distribution reappears. This complete phenomenology is represented by all fitted $r(\varepsilon, T)$ data shown as a color-coded 2D histogram in Fig. 3d. Here, the dashed curve $\bar{\varepsilon}_M(T)$ indicates the average energy of conventional monopole generation-recombination noise[16,17], while the dotted curve $\bar{\varepsilon}_B(T)$ plots the average energy of monopole current bursts ascribed to dynamical

heterogeneity. Measured relative energy intensities of monopole current bursts $\bar{\varepsilon}_B(T)$ and of $\bar{\varepsilon}_M(T)$ are shown in Fig. 3e.

Dynamical heterogeneity theory for conventional supercooled fluids is often based upon the concept of a potential energy landscape (PEL). This is the global potential energy $U(\boldsymbol{r}_N)$ of N-particle configurations, having distinct local minima that are explored dynamically by thermally activated fluctuations[1,2,6,19-24]. In such a PEL context, one would consider thermally activated transitions between heterogeneous monopole-spin configurations separated by energy E. Thus, we evaluate the maximum energy E of each monopole current burst (Methods section 5) as derived from local maxima in $\varepsilon(t)$. Plots of the measured rate of occurrence $R(E,T)$ of events with energy E are presented in Fig. 4a. Here it is conspicuous that $R(E,T)$ always exhibits a distribution exponential in E. Figure 4b shows the complete temperature dependence of $R(E,T)$ where this is borne out. In a PEL context, a highly simplified model for the probability of a transition requiring energy E could be $P(E,T) = N(T) \exp\left(-\frac{E}{kT}\right)/Z$ where $N(T) = N\exp(-\frac{\Delta}{kT})$ is the total number of monopoles in the sample at temperature T, and Z is the PEL partition function. Then, $lnP(E,T) = Const - lnZ - (\Delta + E)/kT$ so that measured $\delta = -\partial lnP(E,T)/\partial(E/kT)$ would have values in the range $\delta \sim 1$ when such a model has validity. Such effects are observed approximately between 450 mK and 250 mK in $Dy_2Ti_2O_7$ as shown in Fig. 4c. Consequently, the PEL concept[1,2,6,19-24], but now for thermally stimulated transitions between monopole-spin configurations separated by E, may provide a novel approach to dynamical heterogeneity deep in the supercooled monopole phase.

Exploration of the noise power-law in the supercooled regime via its power spectral density $S_M(\omega,T) \equiv {C_0}^2 S_V(\omega,T)$ is carried out by fitting to $S_M(\omega,T) \propto \tau(T)/(1 + (\omega\tau(T)^b)$ (Supplementary Fig. 8). The fit values of $b(T)$ are presented in Fig. 5c (iv), showing that for $500 \text{ mK} < T < 1500 \text{ mK}$, $b(T) \cong 1.5$ as expected[9]. A sharp drop in $b(T)$ emerges with falling temperature, eventually reaching values near $b \approx 1$ as $T \to 0$ in regime-III (Methods section 8). Moreover, considering this $T \to 0$ monopole noise, its total power is quantified by the measured variance $\sigma_M^2(T) \equiv \langle M(t)^2 \rangle - \langle M(t) \rangle^2$. As shown in Fig. 5c (v), $\sigma_M^2(T)$ from data in Fig. 5a diminishes through the supercooled regime. However, for $T \lesssim 250 \text{ mK}$, $\sigma_M^2(T)$ reaches a steady non-zero level of approximately 10% of its $T \approx 1500 \text{ mK}$ value. Detailed analysis of $S_M(\omega,T)$ in Fig. 5b reveals that this signal represents persistent monopole noise at approximately 2% of all Dy sites (Methods section 9). This unanticipated phenomenon occurs in the ultra-low temperature regime where the linear-response relaxation time has diverged $\tau \to \infty$. Among possible explanations are quantum dynamical monopoles due to an extended spin-ice Hamiltonian[7], or due to "ghost" spins at absent Dy ions whose adjacent tetrahedra contain a potentially itinerant monopole/antimonopole pair[34].

We amalgamate all the above results on the emerging phenomenology of dynamical heterogeneity in Dy$_2$Ti$_2$O$_7$ spin-ice, in Fig. 5c. Below $T \approx 1500$ mK, intense monopole current bursts emerge whose maximum magnitude relative to the conventional magnetic monopole noise $\mathcal{R} = \max(\varepsilon_B)/\overline{\varepsilon_M}$ grows rapidly, reaching maximum near $T \approx 500$ mK and eventually disappears near $T \lesssim 250$ mK (Fig. 5c (i)). Traversing this supercooled regime, a direct measure of monopole ergodicity $X(\omega, T)$ diminishes cumulatively, reaching a minimum at $T \lesssim 250$ mK (Fig. 5c (ii)). As surmised from their Boltzmann-like statistics (Fig. 4c) thermally activated transitions between monopole-spin configurations of energies E occur for 250 mK $\lesssim T \lesssim 400$ mK (Fig. 5c (iii)). Similarly, the power law of magnetization noise collapses from the expected value[9] $b=1.5$ toward $b=1$ (Fig. 5c (iv)). Although dynamical heterogeneity is suppressed and ergodicity lost by $T \approx 250$ mK where the spin-ice ostensibly enters a glass state, narrowly distributed monopole noise persists for $T \ll 250$ mK (Fig. 5b), implying persistent high frequency monopole dynamics at approximately 2% of Dy sites. Overall, these data provide a far clearer empirical understanding of microscopic dynamics of monopole fluids in Dy$_2$Ti$_2$O$_7$. Many long-anticipated phenomena[7-11] have materialized, including discovery and quantification of dynamical heterogeneity of supercooled monopole fluids (Fig. 3, Fig. 5c) appearing in the form of monopole current bursts (Fig. 2); continuous loss of ergodicity traversing the dynamical heterogeneity regime (Fig. 1c, Fig. 5c), thermal transitions between monopole-spin configurations of energies E apparently within a potential energy landscape (Fig. 4), and persistent high frequency monopole dynamics at $T \to 0$ (Fig. 5a, Fig 5c). Clearly, all five characteristics span the same three ranges: a thermally activated quasi-free monopole fluid (I) in darker blue; the supercooled regime encompassing monopole dynamical heterogeneity (II) in white; and an exceptional regime apparently supporting dynamical monopole matter as $T \to 0$ (III) in light blue. This comprehensive new phenomenology for supercooled monopole fluids (Fig. 5c) can greatly facilitate the development of accurate atomic-scale theories for monopole freezing and thus the true ground state of in spin-ice[7-12,15,28].

Further, the striking correspondence between the phenomenology of dynamical heterogeneity in supercooled monopole fluids (Figs. 2-5) and that in supercooled liquids[1-6] emphasizes the universality of these concepts, and also reveals fundamental new research avenues. Direct access to the time sequence (Fig. 2), energy states (Fig. 3) and thermal statistics (Fig. 4) of dynamical heterogeneity contributes abundant new data to guide and evaluate realistic theories of the supercooled glass-formative process. Indeed, PEL-based theories[1,2,6,19-24] contain many heretofore untestable predictions. For example, the glass fragility index D and relaxation time $\tau(T)$ are determined by the PEL configurational entropy[6,19,20] which, for monopoles, can be controlled directly by external magnetic fields[35]. Or, the time sequence of fluctuating PEL configuration energies due to dynamical heterogeneity, which has long been possible to simulate for different models[22], can now be measured directly for monopoles (Fig. 3). Or, the four-point correlation function $\chi_4(t, T)$

quantifying fluctuations of the conventional correlation function $C(t, T)$ due to dynamical heterogeneity[19,23,24] may now become directly measurable for monopole fluids. Perhaps most radical: by emulating our approach (Figs. 2-4), nanosecond time-resolved electrostatic noise measurements could become a new frontier for vitrification studies of conventional glass forming fluids[1-6,19-27].

Figure 1 Magnetic Monopole Noise Spectrometry
A. Schematic of the experimental apparatus[16,33] we use for detection of dynamical heterogeneity due to magnetic monopole current bursts in the supercooled monopole fluid of $Dy_2Ti_2O_7$.
B. Typical examples of simultaneously measured $Dy_2Ti_2O_7$ magnetic susceptibility $\chi'(\omega, T)$, $\chi''(\omega, T)$ and magnetization noise spectrum $S_M(\omega, T)$ at $T = 700$mK. Complete simultaneous $\chi''(\omega, T)$:$S_M(\omega, T)$ data spanning 15 mK $< T <$ 2500 mK are shown in Supplementary Figs. 3b and 5a.
C. Temperature dependence of simultaneously measured $Dy_2Ti_2O_7$ $S_M(\omega, T)$ and $\chi''(\omega, T)2kT/\omega\pi\upsilon\mu_0$. Evidently, monopole ergodicity parameterized by $X(\omega, T) \equiv S_M(\omega, T)/\{\chi''(\omega, T)2kT/\omega\pi\upsilon\mu_0\}$ diminishes slowly beginning near $T \approx 500$ mK, to be lost manifestly by $T \lesssim 250$ mK. The samples remain demonstrably in good thermal equilibrium with the thermometer and refrigerator down to least 50 mK (see Fig. 5).

Figure 2 Monopole Current Bursts
A. Typical measured time sequences of monopole current magnitudes $|J(t)|$ from Eqn. 4 over a wide range of temperatures spanning the homogeneous monopole fluid regime I, into the supercooled regime II, and finally the $T \to 0$ regime III.
B. Typical measured probability distribution of the monopole current burst magnitudes $|J(t)|$ e.g. in A. The measured monopole currents span an intensity range of approximately five orders of magnitude, with maximum intensity individual events occurring at $T \approx 900$ mK. These data are highly typical of multiple $Dy_2Ti_2O_7$ samples studied.
C. Typical time rate $r_{|J|}$ of monopole current bursts with magnitude $|J|$, measured versus temperature T. The rate of occurrence $r_{|J|}$ of a monopole current with magnitude $|J|$ is defined as the number $\eta(|J|)$ observed in given time interval I: $r_{|J|} \equiv \eta(|J|)/I$.
D. Average measured intensity of monopole current bursts $\overline{|J|}$ versus temperature. Clearly, approaching the supercooled regime below $T \approx 1500$ mK they intensify dramatically, only to fall precipitously reaching a plateau $T \lesssim 250$ mK.

Figure 3 Noise Bifurcation due to Dynamical Heterogeneity
A. Typical example of unprocessed $\Phi_p(t)$ data showing monopole current-burst events, at $T = 700$ mK. The box-car averaged (see Methods section 5) signal is shown in dark green overlayed on the unprocessed $\Phi_p(t)$ data (light green). The identically box-car averaged signal from the empty pickup coil is shown in black.
B. Typical examples of the $\Phi_p^2(t, T)$ from directly measured time dependence of spontaneous magnetic flux $\Phi_p(t)$. This is shown, for example, at temperatures 50 mK, 250 mK, 500 mK, 700 mK, 900 mK, 1500 mK, and 2500 mK.

C. Typical histograms of the measure rate of flux states $r(\varepsilon, T)$ versus ε. We define the rate of occurrence $r(\varepsilon)$ of any state with energy ε as the number $m(\varepsilon)$ observed in given time interval I: $r(\varepsilon) \equiv m(\varepsilon)/I$. Conventional monopole generation-recombination noise with a simple Gaussian distribution persists until $T \approx 1500$ mK. More intense monopole current bursts with far higher energy appear below this temperature resulting in a bimodal distribution of probabilities as shown via histograms at left, and by the fit curves to each histogram shown at right. Eventually below $T \lesssim 250$ mK the bimodal distribution of monopole current burst energies disappears.

D. Monopole noise bifurcation effect in C is presented as a color-coded 2D histogram containing $r(\varepsilon, T)$ versus ε as a function of temperature T. Dashed curve $\bar{\varepsilon}_M(T)$ indicates the average energy of conventional monopole noise, while the while the dotted curve $\bar{\varepsilon}_B(T)$ plots the average energy of monopole current bursts ascribed to dynamical heterogeneity.

E. Relative intensities of average energy of monopole current bursts $\bar{\varepsilon}_B(T)$ and of conventional monopole noise $\bar{\varepsilon}_M(T)$.

Figure 4 Statistical Physics of Monopole Dynamical Heterogeneity

A. Plots of typical measured rate $R(E)$ of monopole current bursts of maximum energy E; e.g. at temperatures 50 mK, 250 mK, 500 mK, 700 mK, 900 mK, 1500 mK and 2500 mK. We define the rate of occurrence $R(E)$ such that when $n(E)$ such events with energy E are observed in a given time interval I: $R(E) \equiv n(E)/I$.

B. Complete temperature dependence of the rate $R(E)$ of monopole current bursts versus E as a function of T.

C. Plotting $lnP(E,T)$ versus E/kT for $250\, mK \lesssim T \lesssim 450\, mK$ reveals an approximate collapse of that subset of data indicative of thermally activated transitions between a range of monopole-spin configurations each with distinct energy E.

Figure 5 Evolution Monopole Dynamical Heterogeneity with Temperature

A. Unprocessed magnetization noise power spectral density $S_M(\omega, T)$ data versus T (processed data and fit quality shown in Supplementary Fig. 5). The measured empty-coil noise floor is plotted as a black curve and lies below the monopole noise spectra.

B. Measured magnetization noise $S_M(\omega, T)$ at high frequency shown for $T < 800$ mK (color code same as A). High frequency noise produced by monopoles decreases with temperature until $T \approx 250$ mK, below which the monopole noise persists unchanged in its temperature or frequency characteristics. The measured empty-coil noise floor is plotted as a grey surface below the monopole noise spectra.

C. (i) Measured ratio of maximal monopole current bursts relative to the conventional magnetic monopole noise $\mathcal{R} \equiv max\, (\varepsilon_B)/\overline{\varepsilon_M}$; (ii) Measured monopole fluid ergodicity $X(\omega, T) = 2k_B T \chi''(\omega, T)/\omega \pi v \mu_0 S_M(\omega, T)$; (iii) Measured thermal activation factor $\delta \equiv -\partial lnP/\partial(E/kT)$ ostensibly between monopole-spin configurations of energy E; (iv)

Measured frequency-dependent power law $b(T)$ of magnetization noise. Below 250 mK $b(T)$ can no longer be extracted from the magnetization noise using Eqn. 4; (v) Measured variance $\sigma_M^2(T)$ of magnetic monopole noise revealing that saturation at approximately 10% of the intensity observed at $T \approx 1500$ mK. Evidently, all five characteristics of magnetic monopole dynamics span the same three ranges of temperature: thermally activated quasi-free monopole fluid (I) indicated in darker blue; the supercooled regime encompassing newly discovered monopole dynamical heterogeneity phenomenology (II) in white; and the exceptional regime revealed to support dynamical monopole matter as $T \to 0$ (III) in light blue.

Author Contributions: J.C.S.D. and J.W. conceived the project. G.L. and S.S. synthesized and characterized the samples; J.C.D, F.J., C.C., C.-C.H, H.T. developed monopole noise spectroscopy technology and carried out experimental measurements; C.D and J.W. administered and supervised research operations at UCC. S.J.B. supervised research operations at OU and provided theoretical guidance. C.C. and J.C.D. developed and carried out the comprehensive analysis with key contributions from C.D. and J.W. J.C.S.D. and J.W. supervised the research project and wrote the paper with key contributions from C.D., C.C. and J.C.D. The manuscript reflects the contributions and ideas of all authors.

Author Information Correspondence and requests for materials should be addressed to jcseamusdavis@gmail.com or jonathan.ward@ucc.ie

References

[1] Berthier, L., Biroli, G., Bouchaud, J.-P., Cipelletti, L. & van Saarloos, W. *Dynamical Heterogeneities in Glasses, Colloids and Granular Media* (Oxford Univ. Press, 2011).

[2] Berthier, L. Dynamic heterogeneity in amorphous materials. *Physics* **4**, 42 (2011).

[3] Biroli, B., Miyazaki, K. & Reichman, D. R. *Spin Glass Theory and Far Beyond*, (World Scientific, 2023).

[4] Ediger, M. D., Angell, C. A. & Nagel, S. R. Supercooled liquid and glasses. *J. Phys. Chem.* 100(31), 13200-13212 (1996).

[5] Tarjus, G., Kivelson, S. A., Nussinov, Z. & Viot, P. The frustration-based approach of supercooled liquids and the glass transition: a review and critical assessment. *J. Phys.: Condens. Matter* **17**, R1173 (2005).

[6] Cavagna, A. Supercooled liquids for pedestrians. *Phys. Reports* **467**, 51-124 (2009).

[7] Rau, J. G. & Gingras, M. J. P. Spin slush in an extended spin ice model. *Nat. Commun* **7**, 12234 (2016).

[8] Udagawa, M., Jaubert, L. D. C., Castelnovo, C. & Moessner, R. Our-of-equilibrium dynamics and extended textures of topological defects in spin ice. *Phys. Rev. B* **94**, 104416 (2016).

[9] Hallén, J. N., Grigera, S. A., Tennant, D. A., Castelnovo, C. & Moessner, R. Dynamical fractal and anomalous noise in a clean magnetic crystal. *Science* **378**, 1218-1221 (2022).

[10] Raban, V., Berthier, L & Holdsworth, P. C. W. Violation of the fluctuation-dissipation theorem and effective temperatures in spin ice. *Phys. Rev. B* **105**, 134431 (2022).

[11] Samarakoon, A. M. et al. Structural magnetic glassiness in the spin ice $Dy_2Ti_2O_7$. *Phys. Rev. Res.* **4**, 033159 (2022).

[12] Kassner, E. R. et al. Supercooled spin liquid state in the frustrated pyrochlore $Dy_2Ti_2O_7$. *Proc. Natl Acad. Sci.* **112**, 8549-8554 (2015).

[13] Rhyzkin, I. A. Magnetic relaxation of rare-earth pyrochlores. *J. Exp. Theor. Phys.* **101**, 481-486 (2005).

[14] Castelnovo, C., Moessner, R. & Sondhi, S. L. Magnetic monopoles in spin ice. *Nature* **451**, 42-45 (2008).

[15] Castelnovo, C., Moessner, R. & Sondhi, S. L. Spin ice, fractionalization and topological order. *Annu. Rev. Condens. Matter Phys.* **3**, 35-55 (2012).

[16] Dusad, R. et al. Magnetic monopoles noise. *Nature* **571**, 234-239 (2019).

17 Samarakoon, A. M. et al. Anomalous magnetic noise in an imperfectly flat landscape in the topological magnet $Dy_2Ti_2O_7$. *Proc. Natl Acad. Sci.* **119**, e2117453119 (2022).

18 Anderson, P. W. Through the glass lightly. *Science* **267**, 1615-1616 (1995).

19 Arceri, F. et al. *Glasses and Aging: A Statistical Mechanics Perspective* (Encyclopedia of Complexity and Systems Science 2022).

20 Adam G. and Gibbs J., *J. Chem. Phys.* **43** 139 (1965).

21 Goldstein, M., *J. Chem. Phys.* **51** 3728 (1969).

22 van Beest, B. W. H., Kramer, G. J. & van Santen, R. A., *Phys. Rev. Lett.* **64** 1955 (1990).

23 Sciortino, F. *J. Stat. Mech.* P05015 (2005).

24 Dalle-Ferrier, C. et al. *Phys. Rev. E* **76**, 041510 (2007).

25 Kawasaki, T. & Tanaka, H. Apparent violation of the fluctuation-dissipation theorem due to dynamic heterogeneity in a model glass-forming liquid. *Phys. Rev. Lett.* **102**, 185701 (2009).

26 Vila-Costa, A., Gonzalez-Silveira, M., Rodríguez-Tinoco, C. et al. Emergence of equilibrated liquid regions within the glass. *Nat. Phys.* **19**, 114-119 (2023).

27 Gerhard, J., Biroli, G. & Berthier, L. Dynamic heterogeneity at the experimental glass transition predicted by transferable machine learning. Preprint at https://arxiv.org/abs/2310.20252 (2023).

28 den Hertog, B. C. & Gingras, M. J. P. Dipolar interactions and origins of spin ice in Ising pyrochlore magnets. *Phys. Rev. Lett.* **84**, 3430-3433 (2000).

29 Ramirez, A. P., Hayashi, A., Cava, R. J., Siddharthan, R. & Shastry, B. S. Zero-point entropy in spin ice. *Nature* **399**, 33-335 (1999).

30 Bramwell, S. T. & Gingras, M. J. P. Spin ice state in frustrated magnetic pyrochlore materials. *Science* **294**, 1495-1501 (2001).

31 Melko, R. G. & Gingras, M. J. P. Monte Carlo studies of the dipolar spin ice model. *J. Phys.: Condens. Matter* **16**, R1277 (2004).

32 Kirschner, F. K. K., Flicker, F., Yacoby, A., Yao, N. Y. & Blundell, S. J. Proposal for the detection of magnetic monopoles in spin ice via nanoscale magnetometry. *Phys. Rev. B* **97**, 140402 (2018).

33 Hsu, C.-C. et. al. Dichotomous Dynamics of Magnetic Monopole Fluids *Proc. Natl Acad. Sci*. **121** (21) e2320384121.

[34] Sen, A., Moessner, R. Topological Spin Glass in Diluted Spin Ice. *Phys. Rev. Lett.* **114**, 247207 (2015).

[35] Ryzhkin, I. A. & Whitworth, R. W. The configurational entropy in the Jaccard theory of the electrical properties of ice. *J. Phys.: Condens. Matter* **9** 395 (1997).
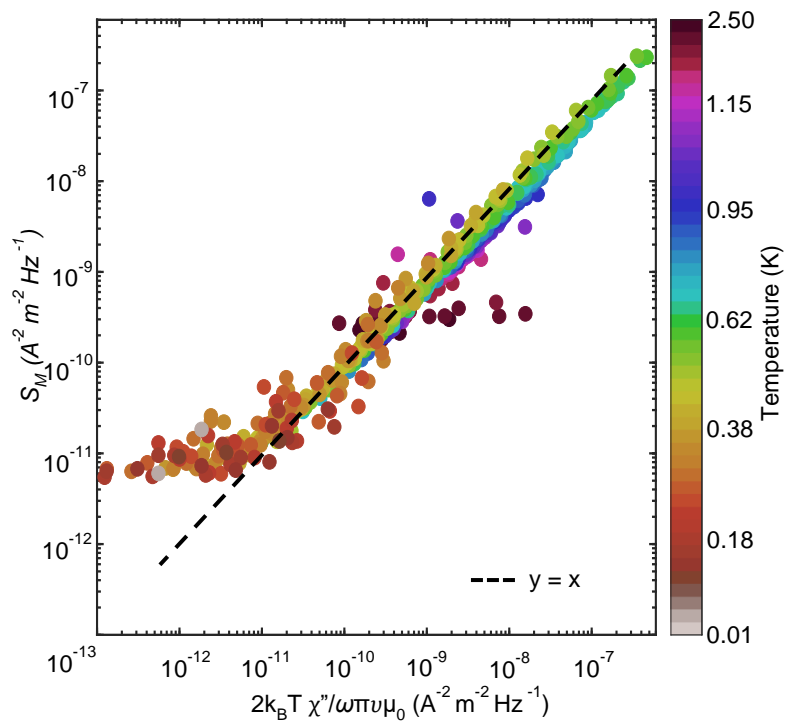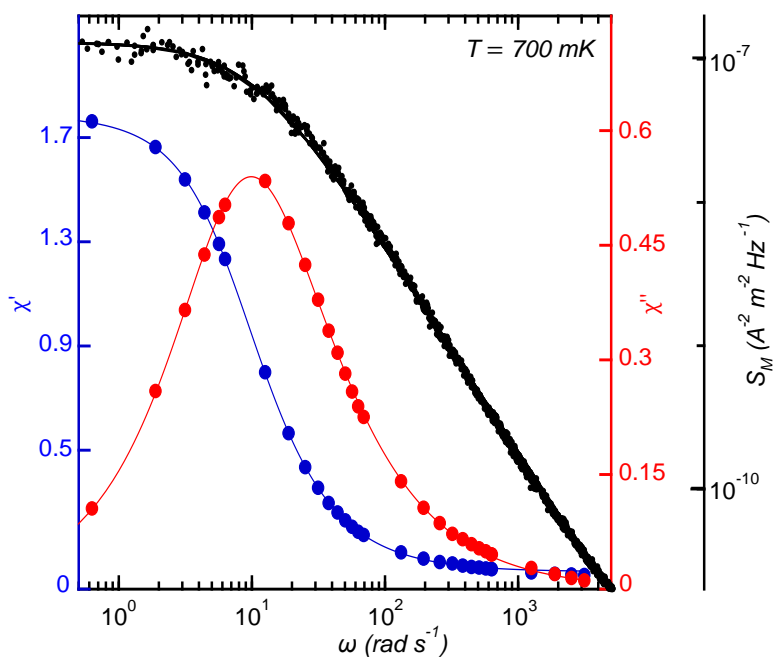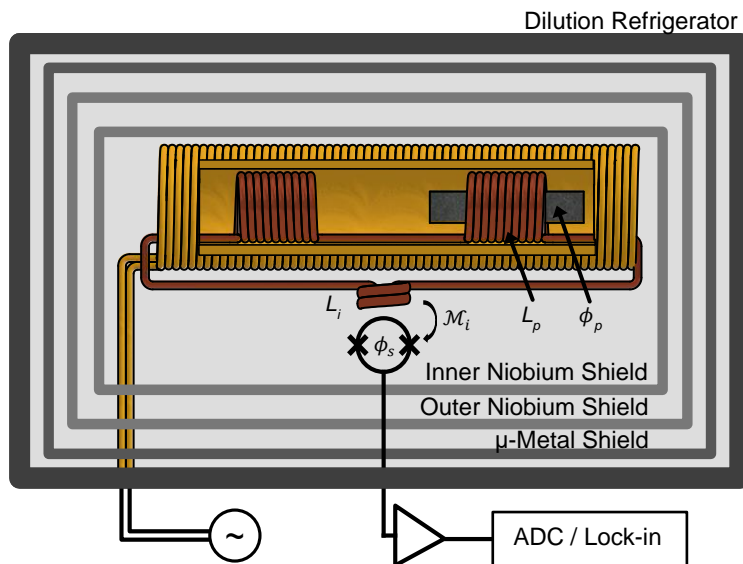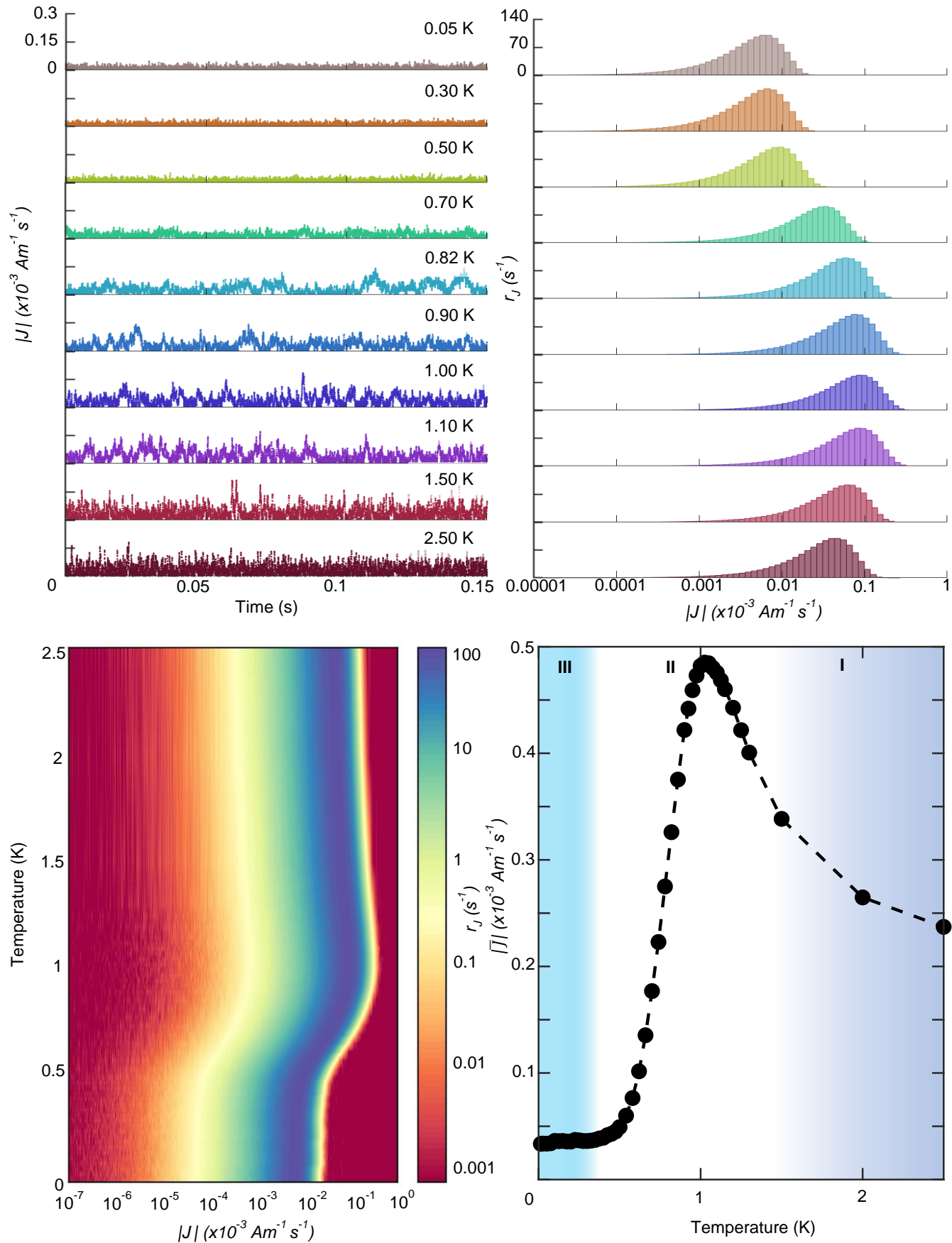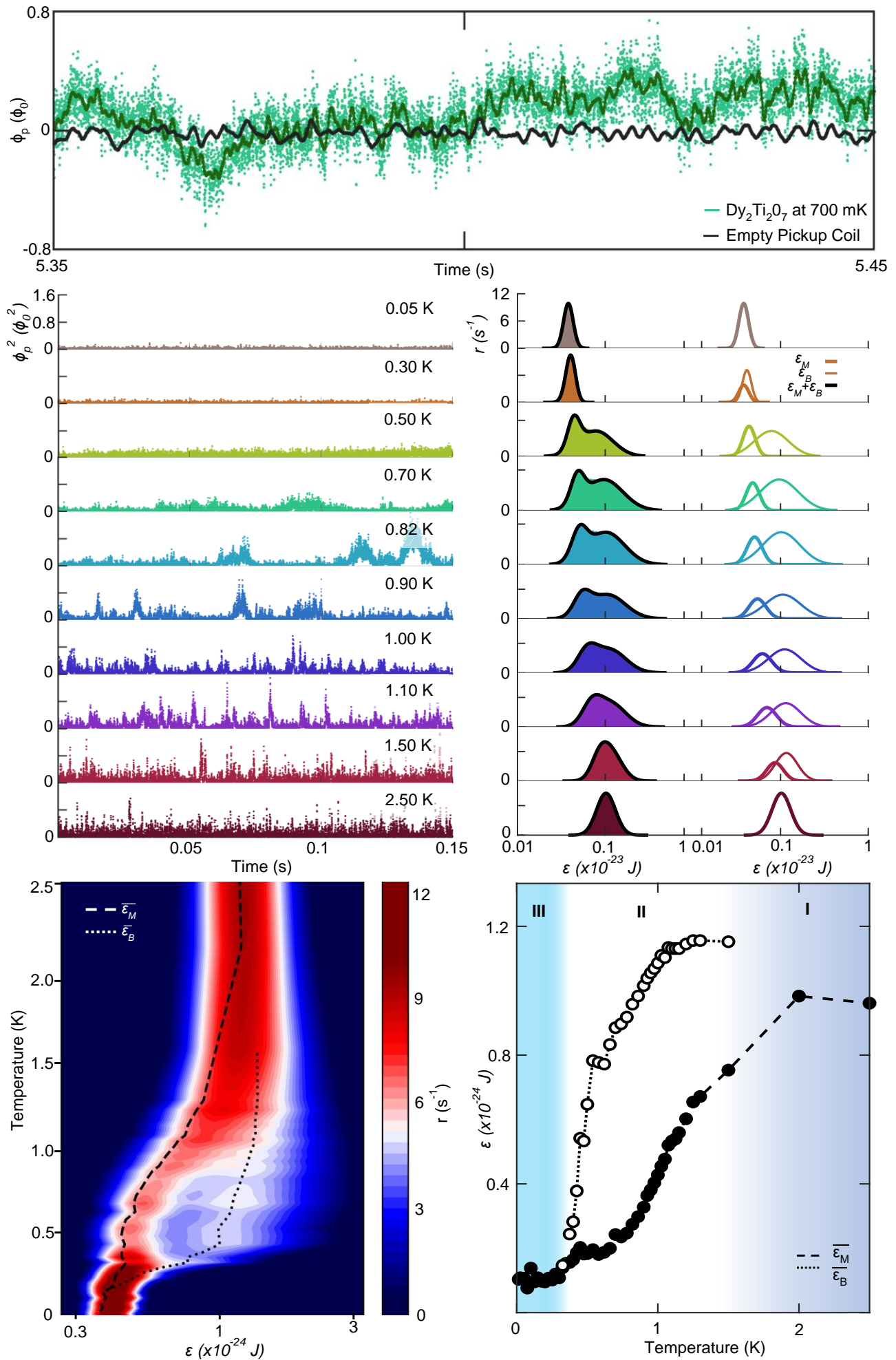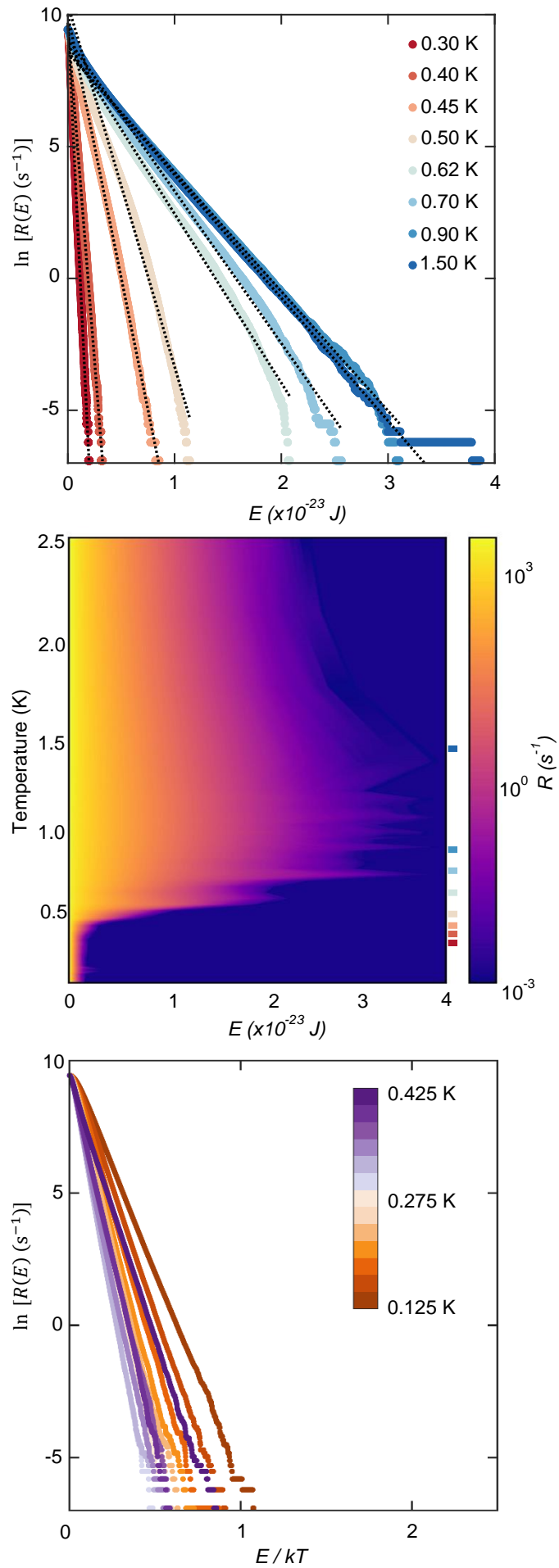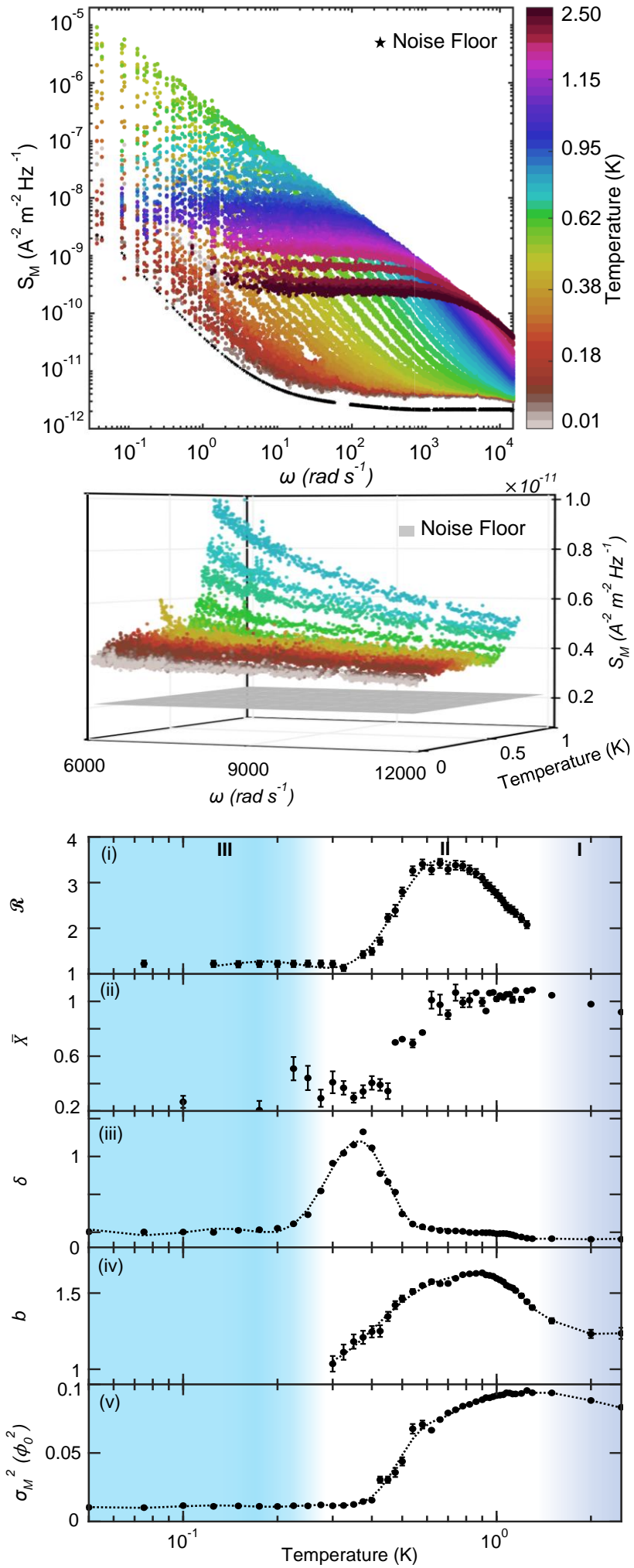
Figure 1

Figure 2

Figure 3

Figure 4

Figure 5

Supplementary Information

1. Susceptibility and Relaxation Time Studies of $Dy_2Ti_2O_7$
Magnetic AC Susceptibility

The magnetic susceptibility $\chi(\omega, T) = \chi'(\omega, T) - i\chi''(\omega, T)$ of $Dy_2Ti_2O_7$ is known empirically with high precision[36-45], as is the fact that below $T \approx 500$ mK the linear-response relaxation rates in $Dy_2Ti_2O_7$ become ultra-slow[46-48]. Supplementary Fig. 1 contains a review of measured linear-response relaxation times of $Dy_2Ti_2O_7$ using different experimental techniques with data from this work included.

Previous high precision studies of the magnetic susceptibility[12] of $Dy_2Ti_2O_7$ identified that the frequency-dependence of the magnetic susceptibility is very accurately parametrized by the Havriliak-Negami (HN) equation[49]

$$\chi(\omega, T) = \chi_\infty + \chi_0(T)/\left(1 + (i\omega\tau(T))^{\alpha(T)}\right)^{\gamma(T)} \qquad (M1)$$

Solving for the real and imaginary components of M1 we find that

$$\chi' = \chi_\infty + \chi_0 \frac{\cos(\gamma\phi)}{\left(1 + 2(\omega\tau)^\alpha \cos\left(\frac{\pi\alpha}{2}\right) + (\omega\tau)^{2\alpha}\right)^{\gamma/2}} \qquad (M2)$$

$$\chi'' = \chi_0 \frac{\sin(\gamma\phi)}{\left(1 + 2(\omega\tau)^\alpha \cos\left(\frac{\pi\alpha}{2}\right) + (\omega\tau)^{2\alpha}\right)^{\gamma/2}} \qquad (M3)$$

Here χ_∞ is the real value of χ in the $\omega \to \infty$ limit, τ is the characteristic relaxation time, α and γ describe the broadening and asymmetry of relaxation times and

$$\phi = \arctan((\omega\tau)^\alpha \sin\left(\frac{\pi\alpha}{2}\right)/1 + (\omega\tau)^\alpha \cos\left(\frac{\pi\alpha}{2}\right)) \qquad (M4)$$

Further, the divergence of linear-response relaxation times derived from M1 was demonstrated to be

$$\tau(T) = A\exp(DT_0/(T - T_0)) \qquad (M5)$$

where $D = 13.6 \pm 5.0$ is the fragility index of the glass-forming state and $T_0 \approx 240$ mK $\pm$ 30 mK. This is the Vogel–Tammann–Fulcher (VTF) form characteristic of a supercooled glass-forming liquid. Hence, these forms for the susceptibility $\chi(\omega, T)$ and the relaxation time $\tau(T)$ identified the existence of a supercooled monopole liquid in $Dy_2Ti_2O_7$, a deduction that is consistent with the empirical $\chi(\omega, T)$ and $\tau(T)$[11,12,16,17,50-52] reported by virtually all studies.

2. Combined Monopole Noise Spectrometer and AC Susceptometer
Design

The monopole noise spectrometer assembly is shown schematically in Supplementary Fig. 2. The sample holder is a hollow Macor cylinder onto which two superconducting coils, signal pick up and field-cancellation coil wound with opposite chirality are connected in-series with the input coil of the SQUID. A cylindrical superconductive 'drive' coil for applying magnetic fields to the sample surrounds the pickup and astatic coil pair. The experiment is mounted at the mixing chamber plate of the dilution refrigerator. A silver wire (0.1 mm diameter) is fixed with GE varnish to the sample inside the sample coil and brought into thermal contact with the temperature sensor, itself screwed to the mixing chamber plate, to ensure reliable thermalization. To expel and then shield external magnetic fields, the SQUID is shielded

within its own Niobium shield, this stage is surrounded by an additional outer Niobium cylindrical shield which is in turn enclosed in a mu-metal shield. This spectrometer is mounted on the mixing chamber plate of a low-vibration cryogen-free dilution refrigerator, vibrationally isolated and enclosed inside an acoustic isolation chamber. The refrigerator reaches a base temperature of 12 mK.

Calibration
The flux at the SQUID input coil is given by
$$V(t) = G\Phi(t) \tag{M6}$$
where $G = 7.31$ V/ϕ_0 is the total gain of the electronics (Supplementary Fig. 2). To calibrate the astatic coil-pair, a cylindrical 1.6 mm diameter Indium sample is chosen for pickup coil calibration and for measuring the imbalance between the pickup and cancellation coils. DC magnetic field sweeps are carried out both above and below the T_c of Indium where the voltage response of the SQUID is given by
$$V_{T>T_c} = C_\chi BA(N_1 - N_2) \tag{M7}$$
and
$$V_{T<T_c} = C_\chi BA(N_1 - N_2(1 - F)) \tag{M8}$$
The Indium rests inside coil two with N_2 turns, $F = 0.57$ is the filling factor of the Indium inside the coil and $C_\chi = 0.0073$ V/ϕ_0 is the transfer function of the SQUID. N_1 is here defined as the number of turns in the cancellation coil, while A represents the cross-sectional area of both the pickup and astatic coils. The ratio N_1/N_2 yields a coil imbalance of ~14%. To measure the true noise floor of the experimental apparatus, the noise is measured with no sample inside the pickup coil. We find the noise floor of the experiment to be 3×10^{-6} $\Phi_0/\sqrt{\text{Hz}}$, as shown in black in Fig. 5a and grey in Fig. 5b.

Noise Acquisition
The time-sequence of the magnetic flux generated by the sample, $\Phi_p(t)$, is extracted using the inductances of the pickup coil L_p and input coil L_i, and $\mathcal{M}_i$ the mutual inductance to SQUID
$$\Phi_p(t) \equiv \Phi(t) / \left(\frac{\mathcal{M}_i}{2L_p+L_i}\right) \equiv V(t)/G\left(\frac{\mathcal{M}_i}{2L_p+L_i}\right) \tag{M9}$$
Using a SR560 Voltage Preamplifier, the signal is amplified and filtered by a low pass filter with a cutoff frequency f_{LP} of 3 kHz, above which the is virtually monopole noise. For temperatures above 600 mK, an additional high pass filter is added with cutoff f_{HP} of 0.03 Hz. The filtered SQUID output voltage V is recorded with 10 microsecond resolution for a total time of 1000 seconds.

Magnetic Susceptibility Data Acquisition
AC susceptibility measurements use a SR830 lock-in amplifier to measure the in-phase and out-of-phase components of the voltage output of the SQUID. An AC magnetic field B_{mod} is driven by the Sine Out function of the lock-in amplifier. This signal (10 mV$_{\text{RMS}}$) passes through a 20 kΩ resistor and RF filter before entering the drive coil (Supplementary Fig. 2). The response of the Dy$_2$Ti$_2$O$_7$ sample is measured by the SQUID and fed into the lock-in amplifier. At each temperature setpoint, four frequency ranges are recorded in succession: $0.1, 0.3, \dots, 0.9$ Hz; $1, 2, \dots, 10$ Hz; $11, 21, \dots, 101$ Hz; $100, 200, 500, 1000$ and 2000 Hz. The

time constant is chosen to be $\tau_{LI} \geq 3(1/f_{\min})$ for the respective frequency ranges. The sensitivity of the lock-in amplifier is set to 20 mV/nA for $T < 600$ mK and 50 mV/nA for $T \geq 600$ mK.

3. Monopole Noise and AC Susceptibility Analysis

Noise Analysis

The magnetization is related to the output voltage of the SQUID as

$$V(t) = \Phi_p(t) \, G \left(\frac{\mathcal{M}_i}{2L_p + L_i} \right) = \frac{M(t)}{C_0} \tag{M10}$$

where $C_0 \equiv \left(\frac{2L_p + L_i}{\mathcal{M}_i} \right) \left(\frac{\Phi_0}{NAF} \right) = 2.1 \; x \; 10^{-9} \, \text{JT}^{-1}\text{V}^{-1}\text{m}^{-3}$ is calibrated accurately for our experimental geometry. The time-sequences of magnetization fluctuations are then recorded from V for each temperature T, from which the power spectral density of magnetization noise $S_M(\omega, T) \equiv C_0{}^2 S_V(\omega, T)$ is derived using

$$S_M(\omega, T) \equiv \lim_{\mathcal{T} \to \infty} \frac{1}{\pi\mathcal{T}} \left| \int_{-\frac{\mathcal{T}}{2}}^{\frac{\mathcal{T}}{2}} M(t) e^{-i\omega t} dt \right|^2 \tag{M11}$$

Magnetic Susceptibility Analysis

To calculate the AC Susceptibility, it is convenient to first define a pre-factor $F_1 = C_\chi (2L_p + L_i)/\mathcal{M}_i$ for converting the SQUID output voltage to magnetic flux in the pickup coil. $C_\chi = 0.0073$ V/ϕ_0 is a value intrinsic to the SQUID electronics, while $L_p = 0.71$ µH and input coil $L_i = 1.74$ µH represent the inductances of the pickup coil and input coil respectively. $\mathcal{M}_i = 1.1 \times 10^{-8}$ ϕ_0/µA represents the mutual inductance of the SQUID circuitry (Supplementary Fig. 2). To then convert flux to B-field, we define a second pre-factor $F_2 = \Phi_0/NAF$. $N = 16$ is the total number of turns in the pickup coil, $A = 3.843 \times 10^{-6}$ m^2 is the cross-sectional area, $F = 0.57$ is the filling factor, while $\Phi_0 = 2 \times 10^{-15}$ Wb is the flux quantum. At each frequency several in-phase (X) and out-of-phase (Y) voltage values are collected from the Lock-In, from which average values V_x and V_y are calculated. Quantitatively accurate real and imaginary magnetic susceptibilities are then found using

$$\chi'(\omega, T) = \frac{V_x(\omega, T)}{B_{mod}} \left(\frac{1}{F_1 F_2} \right) \tag{M12}$$

$$\chi''(\omega, T) = \frac{-V_y(\omega, T)}{B_{mod}} \left(\frac{1}{F_1 F_2} \right) \tag{M13}$$

χ' and χ'' are fitted to the HN equations M2 and M3 respectively and presented in Supplementary Fig. 3 with the quality of the fits indicated by the inset.

4. Ergodicity Measurements from Fluctuation-Dissipation Theorem Analysis

Examining Ergodicity of the Monopole Fluid

If Fluctuation-Dissipation Theorem (FDT) holds for Dy$_2$Ti$_2$O$_7$, the magnetization noise $S_M(\omega, T)$ is directly related to the imaginary AC susceptibility χ'' by

$$S_M(\omega, T) = \frac{2k_B T}{\omega \pi V \mu_0} \chi''(\omega, T) \tag{M14}$$

wherein SI units are used throughout so that $\chi''(\omega, T)$ is unitless. Using measured $S_M(\omega, T)$ and $\chi''(\omega, T)$, the left-hand side of M14 is plotted against the right-hand side for frequencies in the range $0.3 - 2000$ Hz (Supplementary Fig. 4). Each temperature, differentiated by

color in Fig. 1C, contains several points on the curve corresponding to the frequencies used in the experiment. To quantify the validity of the FDT, a ratio $X(\omega, T)$ is defined as

$$X(\omega, T) = \frac{2k_\mathrm{B}T}{\omega \pi V \mu_0} \frac{\chi''(\omega, T)}{S_M(\omega, T)} \quad \text{(M15)}$$

Where $X \approx 1$, the FDT is obeyed and $X < 1$ indicates a violation of FDT due to a loss of ergodicity of the system. To show the temperature evolution, $\overline{X}(T)$ is now defined from $X(\omega, T)$ averaged over all experimental frequencies. $\overline{X}(T)$ is shown in Fig. 5Cii.

5.   Analysis of Time-Resolved Monopole Noise
Flux at Pickup Coil from SQUID Output
The SQUID output voltage signal $V(t, T)$ is recorded with 10 µs precision. $V(t, T)$ is calibrated by the design of the circuit (Fig. 1a) to accurately measure the flux produced by the Dy₂Ti₂O₇ crystal as it threads the pickup coil $\phi_p(t, T)$ as in M9. A typical $\phi_p(t, T)$ signal is shown as green dots in Fig. 3a. For reference, the noise picked up purely by the circuitry (no Dy₂Ti₂O₇ sample) is shown in black.

Magnetic Monopole Current
The monopole current $J(t, T)$ is related to the flux $\phi_p(t, T)$ by

$$J(t, T) \equiv \dot{\Phi}_p(t, T)/\mu_0 \quad \text{(M16)}$$

When calculating the time derivative of a noisy $\phi_p(t, T)$ signal, an 80 µs boxcar average is first applied to suppress artifacts that may arise from numerical differentiation. The derivative $\dot{\phi}_p(t, T)$ is calculated using the Finite-Difference Method:

$$\dot{\phi}_p(t) = \frac{\phi_p(t+\Delta t) - \phi_p(t-\Delta t)}{2\Delta t} \quad \text{(M17)}$$

Finally using M16 $J(t, T)$ is calculated. Once calculated, we consider the magnitude of current noise $|J(t, T)|$, and we observe no net current. In particular, the distribution of occurrence rate $r_{|J|}$, is calculated by considering the number $\eta(|J|)$ of times a given current magnitude $|J|$ occurs in a fixed time interval I: $r_{|J|} = \eta(|J|)/I$. Further analysis examines the mean of monopole current magnitudes $|J|$ versus temperature T. Results of the novel analysis of the magnitude of monopole current $|J(t, T)|$ are presented in Fig. 2. Although not apparent in Fig. 2b, two types of monopole current occur within this current distribution. Rearranging M16 the relation which directly relates $J(t)$ to changes in the flux $\phi_p(t)$ is

$$\mu_0 \int_{t_i}^{t_f} J(t')\, dt' = \phi_p(t_f) - \phi_p(t_i) \quad \text{(M18)}$$

This means that intense current bursts existing over extended time periods produce excursions in $\Phi_p(t)$ far larger than those generated by conventional monopole noise. This effect is seen directly in histograms of $|\Phi_p(t)|$ as show in ED Fig. 5.

Energetics: Continuous Distribution of Energies
To understand the energy scales of the monopole phenomena, the relation

$$\varepsilon(t) \equiv \Phi_p^2(t, T)/2L_p \quad \text{(M19)}$$

is used. From Fig. 3b it can be seen that current bursts, which are large collective increases in the flux always followed by a collective reversal, typically occur on timescales of order ~1 ms, an averaging is applied to the signal - again an 80 µs boxcar average to suppress numerical artifacts. The smoothed, continuous $\Phi_p^2(t, T)$ signal (Supplementary Figs. 6b and

6c) is converted to energy using M19. Analogous to the current, the distribution of the occurrence rate $r(\varepsilon, T)$ is calculated by considering the number $m(\varepsilon)$ of times a given energy ε occurs in the continuous energy signal within a fixed time interval I: $r(\varepsilon) = m(\varepsilon)/I$. The striking emergence of a second gaussian distribution in the range 250 mK $\lesssim T \lesssim 1500$ mK, corresponding to the emergence of current bursts in the Φ_p^2 signal, prompted further analysis: examining the mean energies of each gaussian noise source. To do so, a given $r(\varepsilon, T)$ distribution is fit to a bi-modal model, where the overall distribution is represented by the sum of two unique gaussian functions

$$\varepsilon_M + \varepsilon_B = A_M \exp\left(-\frac{(\varepsilon-\overline{\varepsilon_M})^2}{2\sigma_M^2}\right) + A_B \exp\left(-\frac{(\varepsilon-\overline{\varepsilon_B})^2}{2\sigma_B^2}\right) \tag{M20}$$

Here the subscript M denotes the noise produced by conventional monopole generation-recombination noise and subscript B denotes the noise produced by transient bursts of monopole current. In the cases where this model fails (i.e. one of the distributions goes to zero, or the two gaussians are almost completely overlapping), we infer that the current bursts are no longer present in the signal. Results of the novel analysis of the continuous distribution of energies are presented in Fig. 4.

Energetics: Distribution of Burst Maxima
The maximum energy of each event is analyzed in an attempt to gain further understanding of the underlying physics governing the monopole current bursts. To find the local maxima in $\Phi_p^2(t, T)$ and subsequently the local maxima in energy E, the $\Phi_p^2(t, T)$ signal is filtered by applying a Savitsky-Golay filter (Degree 15, Frame Length 51) and then differentiate using the same method as M17. Here the maxima of the $\Phi_p^2(t, T)$ signal are of primary concern, in particular their locations in time so the use of a filter is purely to suppress numeric artifacts. The zeroes of the function $\dot{\Phi}_p^2(t, T)$ represent the locations in time of the maxima of $\Phi_p^2(t, T)$. The $\Phi_{p,\text{max}}^2$ values at these zeroes are found (Supplementary Fig. 6c) and finally converted to energy E by

$$E \equiv \phi_{p,\text{max}}^2(t, T)/2L_p \tag{M21}$$

The distribution of the occurrence rate $R(E, T)$ is calculated by considering the number $n(E)$ of times an energy maximum with energy E occurs in the continuous energy signal within a fixed time interval I: $R(E) = n(E)/I$. As shown in Fig. 4a, there is an unambiguous $ln(R(E, T)) \propto -E$ relationship, prompting further discussion of Boltzmann statistics being at play in the current burst energy landscape.

6.   Thermal Statistics of Energy States
Toy Model
We first consider a heuristic model for thermally activated transitions through a Potential Energy Landscape[1,2,6,19-23] describing heterogeneous monopole-spin configurations with energy E. The probability of a monopole current burst producing a transition between states separate by E is then given by:

$$P(E, T) = N(T) \exp\left(\frac{-E}{kT}\right)/Z \tag{M22}$$

In this model, $N(T) = N\exp\left(\frac{-\Delta}{kT}\right)$ is the total number of monopoles in the sample at temperature T and Z is an unknown partition function of dynamical heterogeneity states. Taking the logarithm of M21 gives:

$$lnP(E,T) = \text{Const} - \ln Z - (\Delta + E)/kT \quad \text{(M23)}$$

Plotting $lnP(E,T)$ versus E/kT as in Fig. 4b allows for the examination of the energy dependence of $P(E, T)$ by defining

$$\delta(T) = -\partial lnP(E,T)/\partial(E/kT) \quad \text{(M24)}$$

Hence it is expected that $\delta(T) \sim 1$ for temperatures where the model approximately describes the data. The full temperature dependence of the $lnR(E,T)$ vs ε is shown in Supplementary Fig. 7.

7.   Monopole Noise Power Law

Fitting

The magnetization noise power spectrum floor, as measured using an empty pickup coil, is first subtracted from the measured $Dy_2Ti_2O_7$ magnetization noise. The resulting magnetization noise spectrum S_M reveals the true contribution to the magnetization signal from the monopoles. The magnetization noise spectrum S_M is fitted using a least-squares method to the standard equation

$$S_M(\omega,T) = \frac{\sigma_M^2 \tau(T)}{\left(1+(\omega\tau(T))^{b(T)}\right)} \quad \text{(M25)}$$

in the frequency range $0 - 10,000$ rad/s. For optimal fitting, only data greater than two times above the level of the noise floor are included in the fit. The power law exponent $b(T)$, relaxation time $\tau(T)$ and magnetization variance $\sigma_M^2(T)$ are free parameters of the fit. The quality of fit is indicated by the inset of Supplementary Fig. 8. Fig. 5Civ shows the temperature dependence of the monopole noise power law $b(T)$; a sharp decrease from the predicted $b = 1.5$ towards $b = 1$ is seen in the T → 0 limit.

8.   Dynamical Monopoles as $T \to 0$

Trapped Monopoles

To estimate the fraction of monopoles with apparently persistent dynamics in $Dy_2Ti_2O_7$ at low temperatures approaching 10 mK, we first calculate the variance $\sigma_\Phi^2 = \langle \phi_p{}^2 \rangle - \langle \phi_p \rangle^2$ from the flux time series data. This is shown in Fig. 5Cv. The noise fraction of monopoles $f_{\sigma^2}(T)$ is given by

$$f_{\sigma^2}(T) \approx \frac{\sigma_\Phi^2(T)}{\sigma_\Phi^2(1.5K)} \quad \text{(M26)}$$

In the $T \to 0$ limit, the measured f_{σ^2} tends to $10\% \pm 3\%$ (Supplementary Fig. 9). Magnetic monopoles, with a spin flip energy cost $\Delta \approx 4.35$ K, occupy Dy sites with a number density[53]

$$\rho_N(T) = \frac{2\exp(-\Delta/T)}{1+2\exp(-\Delta/T)} \quad \text{(M27)}$$

Thus $\rho_N(T \to 0)$ tends to $\rho_N(T = 1.5K)\sqrt{f_{\sigma^2}}$, or 2% of all Dy sites This phenomenon is common to all $Dy_2Ti_2O_7$ samples in our study.

## 9. $Dy_2Ti_2O_7$ Samples

Sample Growth

The single crystal $Dy_2Ti_2O_7$ samples are grown by floating zone method. High purity (99.99%) Dy_2O_3, and TiO_2 are mixed and heated to 1400 °C for 40 hours. The mixture is ground immediately, then heated for 12 hours. The resulting powder is packed into a rod, then sintered at 1400° C for 12 hours. A long piece of the sintered rod is used as a feed rod while a small piece is used as the seed. The crystals are grown in 0.4 MPa oxygen pressure at

4 mm/hour using a two-mirror NEC furnace where the feed and seed rods are counter-rotated at 30 rpm.

Repeatability

This sequence of experiments was repeated with multiple different $Dy_2Ti_2O_7$ samples. Modulo their different sizes, all samples produced equivalent phenomenologies (Supplementary Fig. 9).

36 Snyder, J. et al. Low-temperature spin freezing in the $Dy_2Ti_2O_7$ spin ice. *Phys. Rev. B* **69**, 064414 (2004).

37 Matsuhira, K. et al. Spin dynamics at very low temperatures in spin ice $Dy_2Ti_2O_7$. *J. Phys. Soc. Jpn* **80**, 123711 (2011).

38 Bovo, L., Bloxsom, J. A., Prabhakaran, D., Aeppli, G. & Bramwell, S. T. Brownian motion and quantum dynamics of magnetic monopoles in spin ice. *Nat. Commun* **4**, 1535-1542 (2013).

39 Yaraskavitch, L. R. et al. Spin dynamics in the frozen state of the dipolar spin ice $Dy_2Ti_2O_7$. *Phys. Rev. B* **85**, 020410 (2012).

40 Snyder, J., Slusky, J. S., Cava, R. J. & Schiffer, P. How 'spin ice' freezes. *Nature* **413**, 48-51 (2001).

41 Shi, J. et al. Dynamical magnetic properties of the spin ice crystal $Dy_2Ti_2O_7$. *J. Magn. Magn. Mater.* **310,** 1322-1324 (2007).

42 Borzi, R. A. et al. Intermediate magnetization state and competing orders in $Dy_2Ti_2O_7$ and $Ho_2Ti_2O_7$. *Nat. Commun* **7**, 12592 (2016).

43 Yadav., P. K. & Upadhyay, C. Quantum criticality in geometrically frustrated $Ho_2Ti_2O_7$ and $Dy_2Ti_2O_7$ spin ices. *J. Magn. Magn. Mater.* **482**, 44-49 (2019).

44 Takatsu, H. et al. Universal dynamics of magnetic monopoles in two-dimensional Kagomé ice. *J. Phys. Soc. Jpn* **90**, 123705 (2021).

45 Matsuhira, K., Hinatsu, Y. & Sakakibara, T. Novel dynamical magnetic properties in the spin ice compound $Dy_2Ti_2O_7$. *J. Phys.: Condens. Matter* **13**, L737 (2001).

46 Giblin, S., Bramwell, S. T., Holdsworth, P. C. W., Prabhakaran, D. & Terry, I. Creation and measurement of long-lived magnetic monopole currents in spin ice. *Nat. Phys.* **7** 252-258 (2011).

47 Orendáč, M. et al. Magnetocaloric study of spin relaxation in dipolar spin ice. *Phys. Rev B* **75**, 104425 (2007).

48 Revell, H. M. et al. Evidence of impurity and boundary effects on magnetic monopole dynamics in spin ice. *Nat. Phys.* **9**, 34-37 (2013).

49 Havriliak, S. & Negami, S. A complex plane representation of dielectric and mechanical relaxation processes in some polymers. *Polymer* **8**, 161 (1967).

50 Eyvazov, A. B. et al. Common glass-forming spin-liquid state in the pyrochlore magnets $Dy_2Ti_2O_7$ and $Ho_2Ti_2O_7$. *Phys. Rev. B* **98**, 214430 (2018).

51 Pomaranski, D. et al. Absence of Pauling's residual entropy in thermally equilibrated $Dy_2Ti_2O_7$. *Nat. Phys.* **9**, 353-356 (2013).

52 Paulsen, C. et al. Far-from-equilibrium monopole dynamics in spin ice. *Nat. Phys.* **10**, 135–139 (2014).

53 Castelnovo, C., Moessner, R. & Sondhi, S. L. *Phys. Rev. B* **84**, 144435 (2011).

54 Klyuev, A., Ryzhkin, M. & Yakimov, A. Statistics of Fluctuations of Magnetic Monopole Concentration in Spin Ice. *Fluct. and Noise Lett.* **16**, 1750035 (2017).
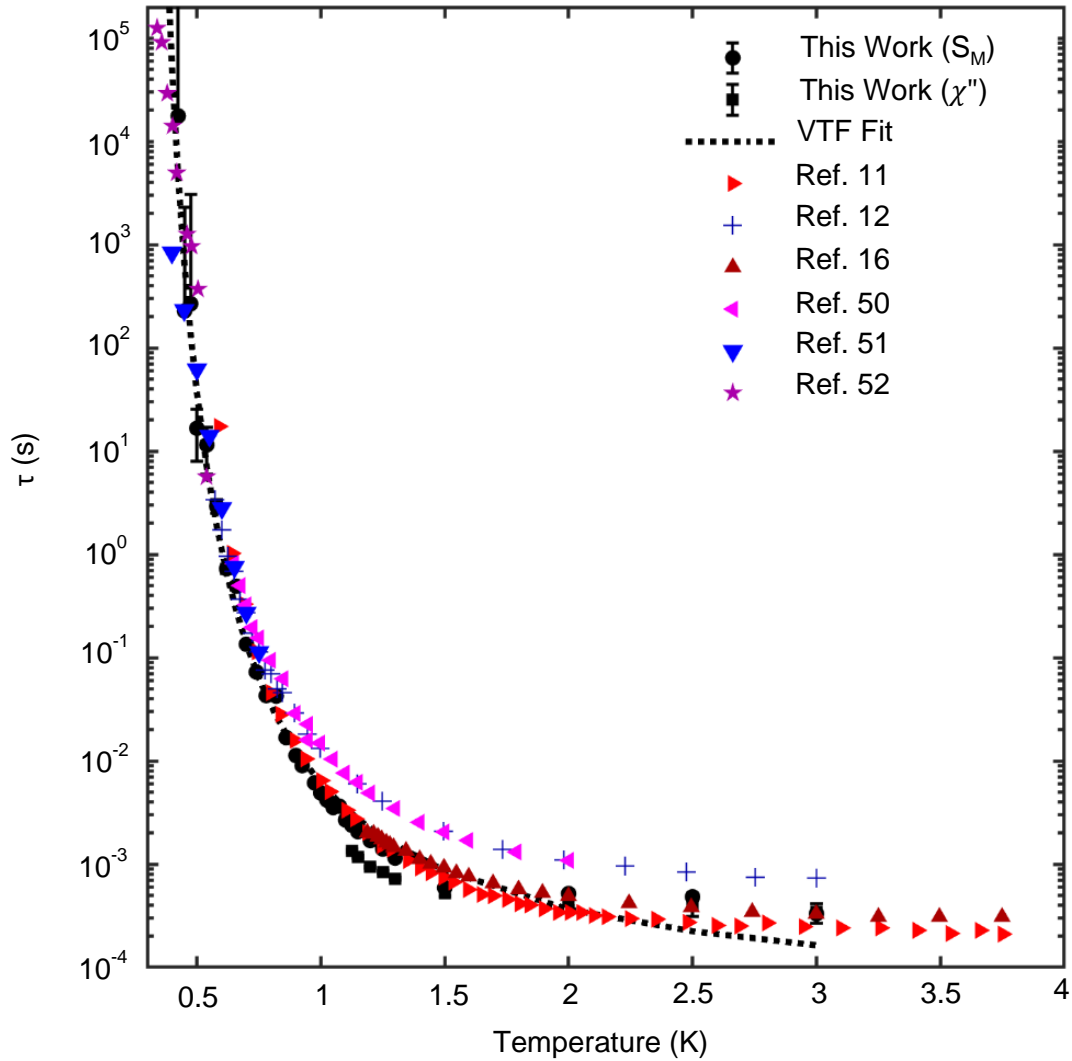
Supplementary Figure 1: Divergent linear-response relaxation time of $Dy_2Ti_2O_7$.

The linear-response relaxation time τ measured by fitting our magnetization noise S_M (black circles) and AC susceptibility χ'' (black squares) is compared to related measurements in the literature (coloured symbols) and found to be consistent with previously reported values. Below $T \approx 500$ mK, τ becomes inaccessible to linear-response experiments due to its divergent behavior approaching $T_0 = 240 \pm 30$ mK.
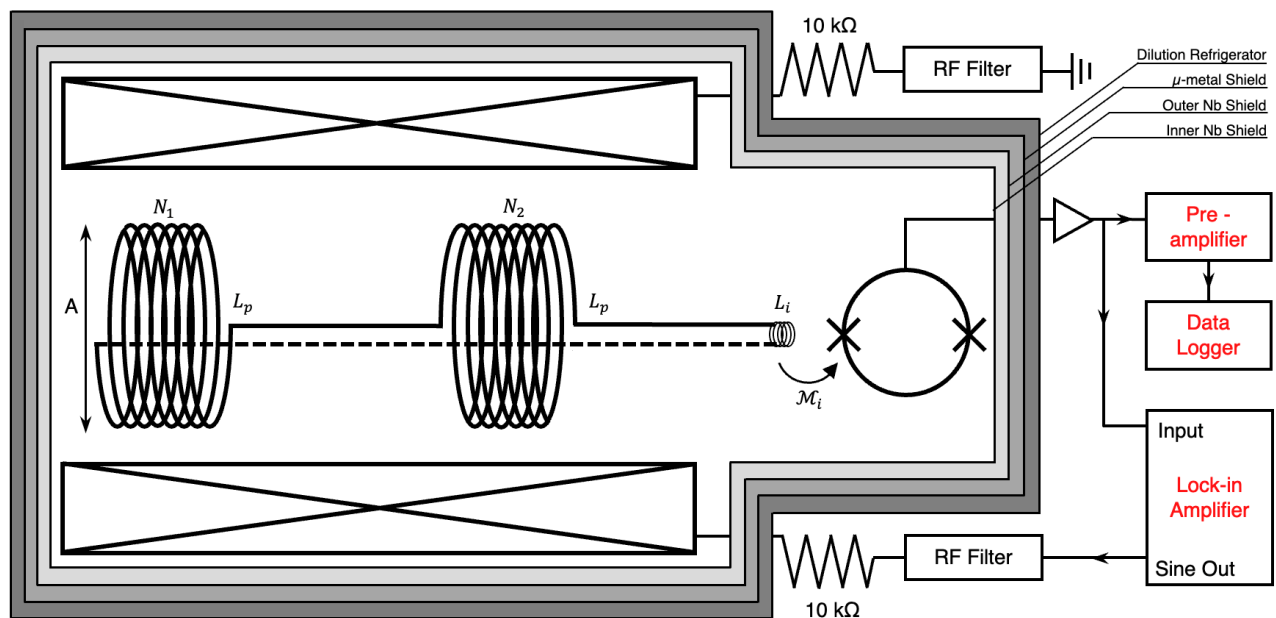
Supplementary Figure 2: Experimental setup.

The schematic of our combined monopole noise spectrometer and AC susceptometer. The circuit diagram illustrates the simultaneous monopole flux-noise and AC susceptibility measurement.
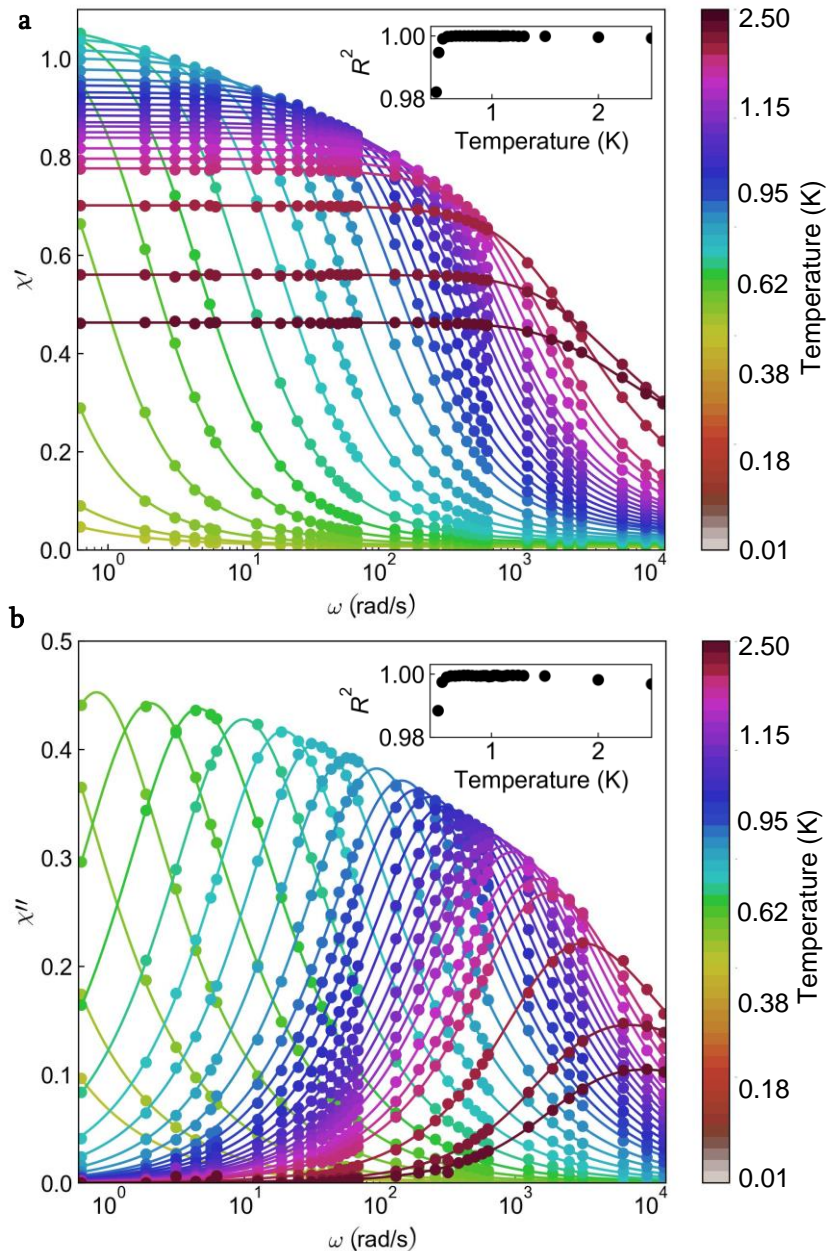
Supplementary Figure 3: Frequency and temperature dependence of the AC susceptibility.

a) The real component of the magnetic AC susceptibility $\chi'(\omega, T)$ is fitted to its parametric equation M2. Below 500 mK the fit fails ($R^2 < 0.95$). b) The imaginary component of the magnetic AC susceptibility $\chi''(\omega, T)$ is fitted to its parametric equation M3. The evolution of the monopole linear-response relaxation time is reflected clearly by the shift of the peak in $\chi''(\omega, T)$ towards lower frequencies as the temperature is decreased. Below 500 mK, where the peak is no longer in our experimental window, the fit fails ($R^2 < 0.95$). Data that cannot be parametrized by M3 are included in Supplementary Fig. 4.
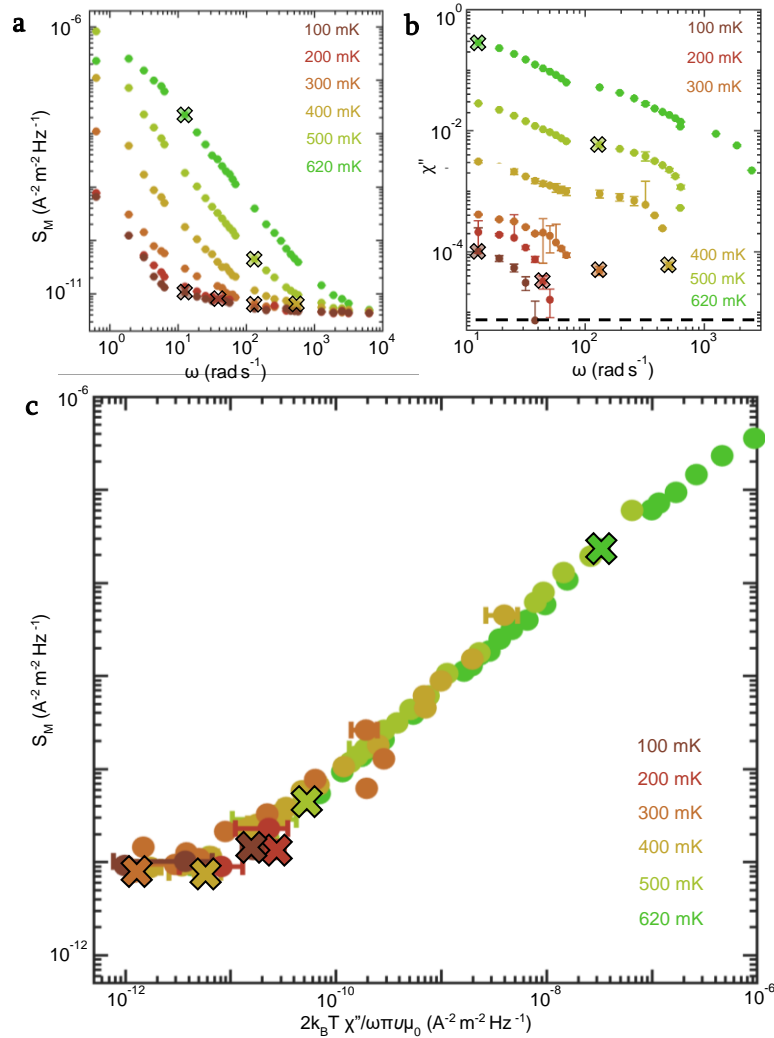
Supplementary Figure 4: Loss of ergodicity in $Dy_2Ti_2O_7$.

a) Magnetization noise S_M at 100 mK, 200 mK, 300 mK, 400 mK, 500 mK, and 620 mK. Each curve shows magnetization noise data at the corresponding frequencies to the susceptibility measurements in the next panel. The error in the noise is less than 1% of the signal in all cases, so the error bars are not included beyond this panel. b) Imaginary susceptibility χ'' at the same temperatures as panel a). The experimental noise floor is plotted at the base of the figure. c) The left-hand side of the fluctuation-dissipation relation M14 (Y) is compared against the right-hand side (X). One data point at each temperature is represented by an 'X' as a guide to the eye. The same points are highlighted in panel a) and b) to identify the pair of unprocessed noise and susceptibility values yielding that data point. At temperatures below 300 mK, a violation of the fluctuation-dissipation theorem is observed, as the linear relationship between the simultaneously measured magnetization noise and imaginary susceptibility fails.
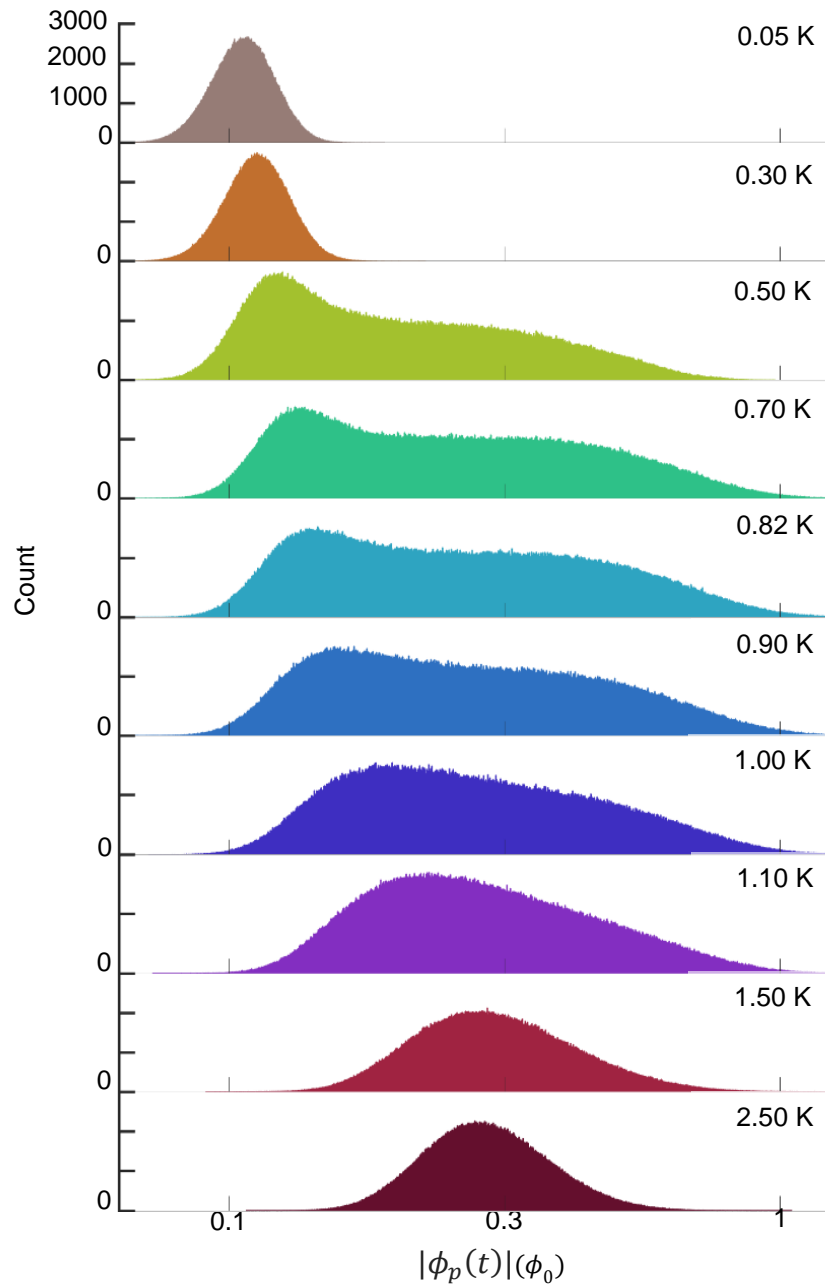
Supplementary Figure 5: Emergence of two maxima in the monopole current

Typical histograms of $|\phi_p(t)|$. Conventional monopole current with a single Gaussian distribution persists until T ≈ 1500 mK. A second current source, due to intense monopole current bursts appears below this temperature resulting in a bimodal distribution of probabilities. Below T ≲ 250 mK the current bursts disappear.
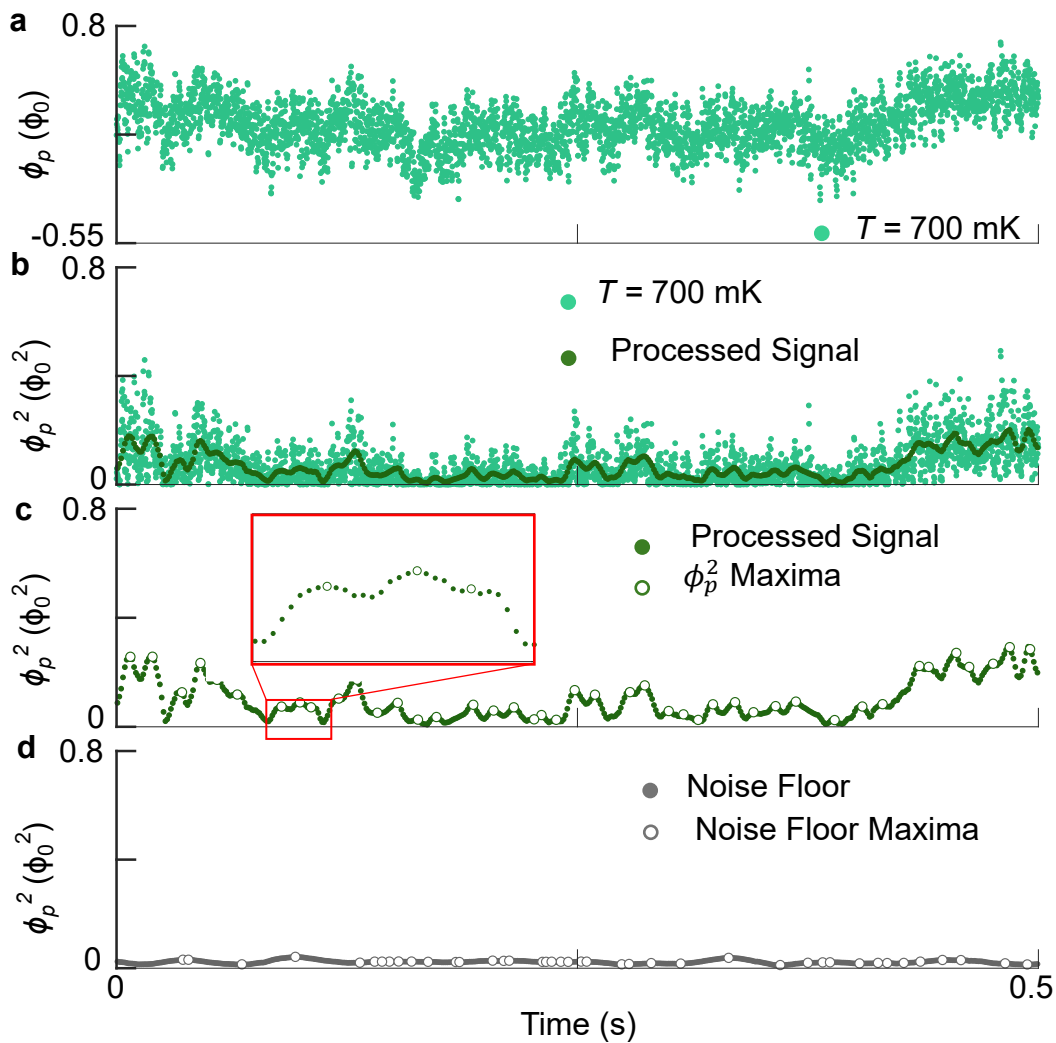
Supplementary Figure 6: Extracting Energies from Typical Flux Time Series.

Note that $\phi_p{}^2$ and energy are considered equivalent here due to their linear relationship as described in equation M19. a) A typical flux signal ϕ_p measured at 700 mK. b) The square of the flux signal $\phi_p{}^2$ is calculated and the signal is then averaged in a 80 μs window. The averaged signal is layered on top of $\phi_p{}^2$. c) The averaged signal is numerically differentiated and the maxima are found and shown above. d) The same routine is applied to the empty coil signal. The flux signal is considerably reduced in the empty coil data.
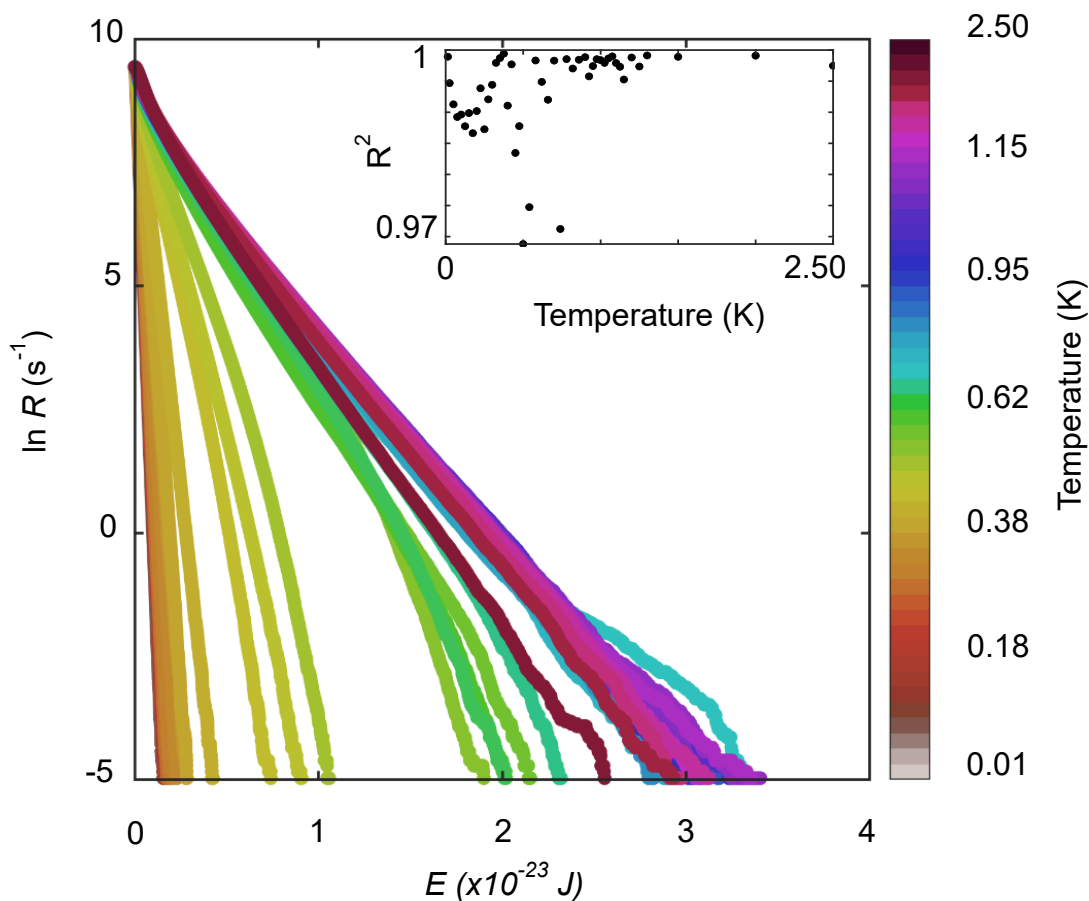
Supplementary Figure 7: Boltzmann statistics of monopole burst energies.

The full temperature dependence of the monopole current bursts shows first an increase in the burst energies which begins upon entering the supercooled regime from the free monopole regime (decreasing in temperature). Then, there is a collapse of burst events as temperature further decreases within the supercooled regime. And finally the low-temperature boundary of dynamical heterogeneity, begins at temperatures below 300 mK.
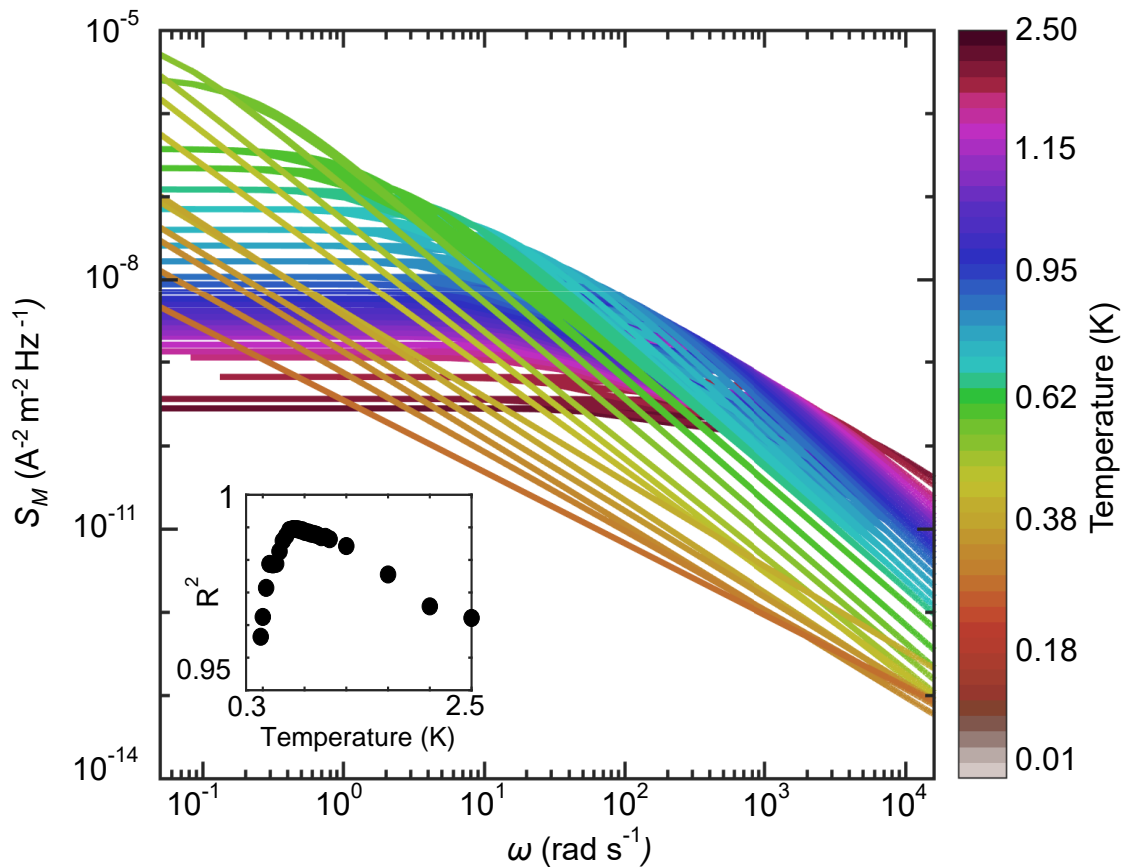
Supplementary Fig 8: Temperature and frequency dependence of fitted magnetization noise S_M.

Fitted magnetization noise power spectral density $S_M(\omega, T)$ data versus T. The noise is well described ($R^2 > 0.95$) by monopole generation/recombination above 300 mK. Below this temperature, fits are excluded.
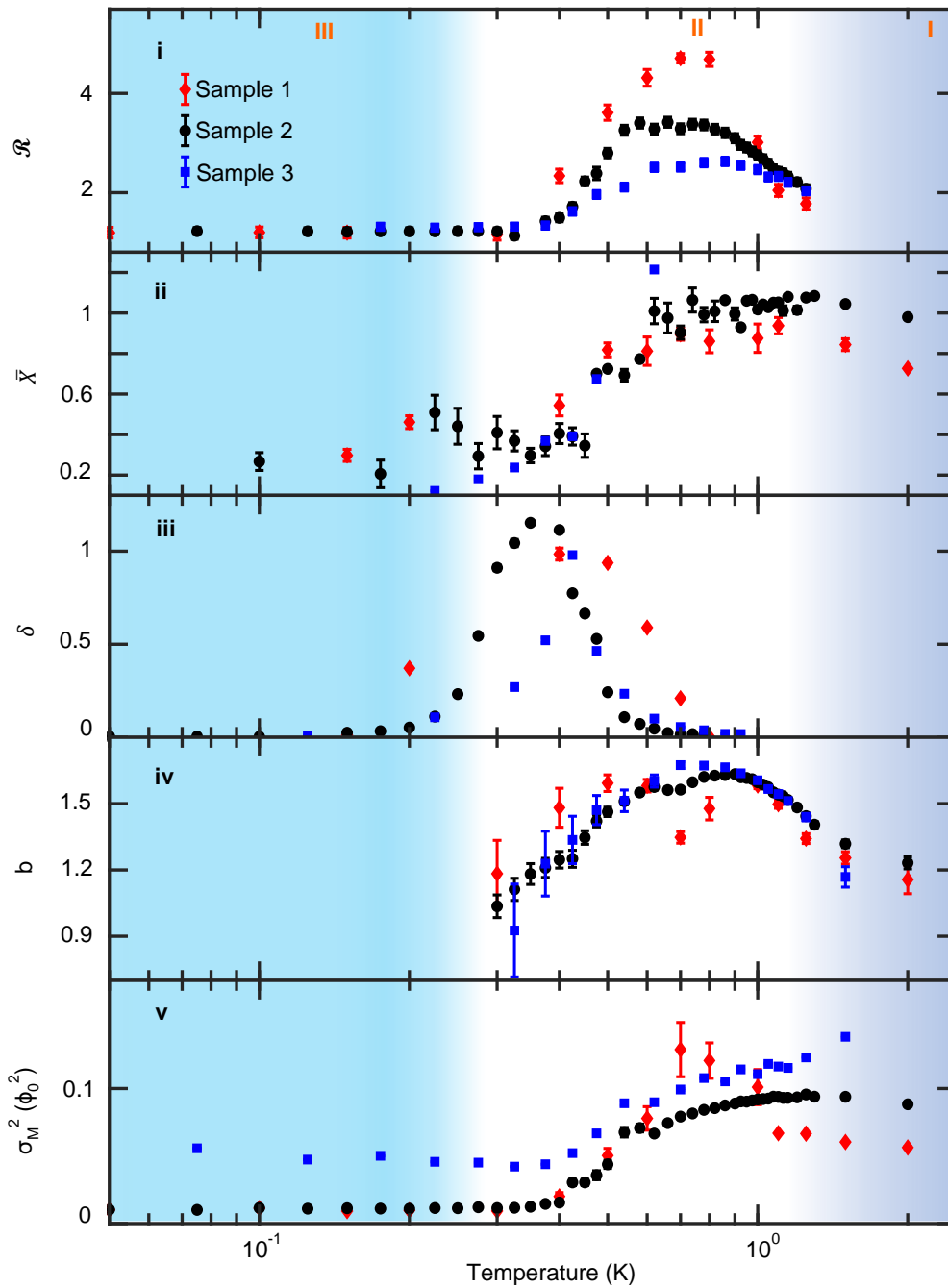
Supplementary Figure 9: Comparison of phenomenologies from different samples.

Each sample studied in this work produced the same phenomenologies, demonstrating qualitative repeatability of the experiment. Changes in magnitude of the noise can be attributed to geometric differences between samples.